An investigation into the variability of methanol and hydroxyl masers in the star-forming region G12.89+0.49

Mihloti Christina Langa (B.Sc., B.Sc.(Hons.))

Thesis submitted in the Department of Physics of the University of North-West University (Potchefstroom Campus) in partial fulfilment of the requirements for the degree of Magister Scientiae.

Supervisors: Dr. S. Goedhart, Dr. M. J. Gaylard and Prof. D. J. van der Walt

Hartebeesthoek Radio Astronomy Observatory

July 30, 2007

An investigation into the variability of methanol and hydroxyl masers in the star-forming region G12.89+0.49

M. C. Langa

July 30, 2007

Abstract

It is now widely accepted that 6.7 GHz and 12.2 GHz class II methanol masers are signposts of very young high mass star-forming regions. The exact location of these masers is still a matter of debate, they may be in disks or shocks near these objects. Hydroxyl masers also show strong emission at 1665 MHz in these regions. They may be excited by the same mechanisms as the methanol masers. Both maser species sometimes show variability. The information from maser variability can be useful in determining conditions and physical changes occurring in these regions.

A daily monitoring program was set up to study the variability of methanol and hydroxyl masers in the G12.89+0.49 star-forming region. G12.89+0.49 is one of the 54 sources monitored by Goedhart et al. (2004). It had shown a flickering behaviour which was not fully characterised, hence the current obervations were undertaken. Methanol masers were observed at 6.7 GHz and 12.2 GHz and hydroxyl masers at 1665 MHz using the 26-m telescope at Hartebeesthoek. The results show that the methanol maser exhibits regular variability with a period between 29 and 30 days. The hydroxyl masers show a little variability.

Opsomming

Dit word nou algemeen aanvaar dat astrofisiese 6.7 en 12.2 GHz metanol masers uitsluitlik met baie jong swaar sterre geassosieer is. Een van die onopgeloste probleme rakende hierdie masers is die vraag na waar in die omgewing van die jong ster die masers voorkom. 'n Verskeidenheid van moontlikhede is al voorgestel, byvoorbeeld, in akkresieskywe, skokke of in vinnig uitvloeiende materiaal wat deur 'n spuitstraal, wat op die akkresieskyf ontstaan, saamgesleep word. Een van die eienskappe van die masers wat kan bydra om die vraag na waar die masers ontstaan te beantwoord, is die tydsveranderlikheid van die masers. 'n Studie van die tydsveranderlikheid van die masers kan waardevol wees om die verandering in die fisiese omgewing waar die masers voorkom, te bepaal en daarmee ook saam waar die masers voorkom.

In hierdie verhandeling word die tydsveranderlikheid van die maserbron G12.89+0.49 bestudeer. Hierdie maserbron is een van die 54 maserbronne wat Goedhart et al. (2004) oor 'n vier jaar tydperk gemoniteer het. G12.89+0.49 het 'n flikkergedrag getoon wat anders was as die tydsveranderlikheid van die meeste ander maserbronne en wat dus verdere ondersoek geverg het. 'n Program om die 6.7- en 12.2 GHz metanolmasers en die 1665 MHz hidroksielmasers in G12.89+0.49 te monitor is opgestel en die masers is vir 'n tydperk van 10 maande gemonitor. Die resultate het gewys dat die flikkergedrag van die 6.7 GHz metanolmasers eintlik 'n periodiese tydsveranderlikheid met 'n periode van tussen 29 en 30 dae is. Geen periodiese veranderlikheid is vir die 1665 MHz hidroksielmasers gevind nie. 'n Verdere analise het aangetoon dat die verskillende 6.7 GHz metanolmasers in G12.89+0.49 in fase en met geen tydsvertraging verander.

Acknowledgements

I wish to thank the NASSP committee for giving me an opportunity to register for an MSc in Astrophysics and Space Science. I wish to thank my supervisors Dr. S. Goedhart, Dr. M. Gaylard and Prof. D. J. van der Walt for patiently guiding and supporting me throughout this dissertation. In addition, I wish to dedicate special thanks to Dr. S. Goedhart for always been there to listen to my complaints and frustrations during stressful moments. Her encouragement, friendship and mentorship can indeed be seen through this dissertation. I wish to thank M. West for proof-reading the thesis. I also wish to thank HartRAO staff for the moral support they gave me throughout the thesis. Lastly, I wish to thank my family: my parents for giving me life, my grandparents for educating me even though it was very difficult, my husband Ondego for his unconditional support and encouragement since the day we met, my dearest son Ondego Junior for being there to cheer me up, giving me company and providing more meaning to my life.

Contents

List of Figures

List of Tables

Chapter 1

Introduction

Understanding the processes of high mass star formation is essential since these stars have a great influence on the evolution of galaxies and the interstellar medium through their powerful ultraviolet (UV) radiation, stellar winds and supply of heavy elements at the end of their lives. Unfortunately a significant amount of information about the process of high mass star formation is still incomplete. This lack of knowledge is a result of the environments in which high-mass star formation occurs. High-mass star forming regions are found at large distances, the nearest being at 450 pc from the Sun (viz Orion). These regions are also enshrouded by dust and gas which blocks the radiation at optical wavelengths. In addition, high-mass stars are formed not in isolation but in clusters where it might be difficult to identify and locate the individual protostars (Carpenter, 2000).

Maser emission from hydroxyl, methanol and water molecules seems to be associated with active regions of high-mass star formation (De Buizer et al., 2005a). These masers are characterised by their small size, high brightness temperature and narrow linewidths. Observations of masers associated with the regions of high mass star formation may be used to to probe the physical conditions (e.g density, luminosity and temperature) and kinematics of the dense gas surrounding the newly formed high mass stars.

Methanol masers have been classified into two groups (Menten, 1991b). Class I methanol masers are not only associated with high mass star forming regions but also with low mass star forming regions. In contrast, class II methanol masers are associated only with regions of high mass star formation (Beuther et al., 2002; Ellingsen, 2006). Class II methanol masers and hydroxyl masers are known to be spatially associated (Gaylard & MacLeod, 1993; Caswell, 1997). The association of the two maser species has led other researchers to suggest that the two masers may be radiatively pumped by the same infrared radiation field (Cragg et al., 2002).

Maser emission from methanol and hydroxyl molecules often shows variability. The observed features may vary on a time scale from days up to years. Studies of variability of masers in high mass star forming regions are important as they may reveal the properties of the gas surrounding such regions. The variability of masers associated with high mass star forming regions may also provide information about the innermost regions around young high mass stars and the various pumping mechanisms of masers.

A study of the variability of methanol masers was done by Goedhart et al. (2004) using a sample of 54 sources. Different variability characteristics such as periodic, quasi-periodic and aperiodic were reported, with other sources showing little or no intensity variations. The G12.89+0.49 star-forming region is one of the sources reported to show weak variability. One of the features was found to show a flickering behaviour which had not been fully sampled by the fortnightly monitoring. Calibration errors were ruled out as a possible cause of the flickering. Apart from methanol masers, the G12.89+0.49 star-forming region also shows hydroxyl maser emission.

This work presents a detailed investigation and analysis of the short term variability of methanol and hydroxyl masers in the G12.89+0.49 star-forming region. The presence of both methanol and hydroxyl masers in the G12.89+0.49 allow a valued examination of the behaviour of the two maser species as well as a comparison of the different models of the variability of the masers. Daily observations were made using the 26-m telescope at HartRAO. These observations were taken at 6.7 GHz and 12.2 GHz for methanol masers and 1665 MHz for hydroxyl masers. The observations aim to further investigate the flickering behaviour reported by Goedhart et al. (2004) and to investigate possible mechanisms of variability of masers.

The thesis is organised as follows: chapter 2 gives a brief overview of high mass stars along with the formation processes. It discusses the characteristics of the surrounding environments, e.g HII regions and masers. The characteristics include the association of masers with other tracers of high mass star forming regions and the location and variability of the masers. Chapter 3 discusses the reasons for selecting the G12.89+0.49 star-forming region. Previous studies towards the target source are discussed. The source G351.42+0.64 selected as a reference for the G12.89+0.49 observations is also discussed. Chapter 4 discusses the observations undertaken and data reduction. The results are presented in Chapter 5 along with the description of the data analysis methods used. Chapter 6 discusses the results and gives conclusions.

Chapter 2

High Mass Star Formation

2.1 Introduction

High mass stars, i.e. stars of spectral type O and B (mass $\gtrsim$8 $M_\odot$) play an important role in shaping the complex interactions of components of galaxies such as dust and gas. From the moment they are formed and throughout their short lives, high mass stars are involved in the production of large amounts of high energy ultraviolet (UV) radiation and powerful stellar winds which ionise and stir up the interstellar gas and dust surrounding them. At the end of their lives they undergo a unique process whereby they explode as supernovae releasing huge amounts of energy. During this process, heavy elements which cannot be formed under a normal nuclear fusion reaction, are produced. These elements are forcefully spread through their surroundings enriching the interstellar medium (ISM) and hence affecting the next generation of stellar chemistry. The shock waves from the supernovae can sweep up the ISM, forming new molecular clouds or triggering a new wave of star formation. Thus, knowledge of high mass star formation and its effects on the surrounding environment is required in order to understand the evolution of galaxies.

Despite the major role high mass stars play, the manner in which they are formed is still not well understood. There are currently two possible models of high mass star formation that have been proposed. Section 2.2 discusses the formation process of high mass stars and the shortcomings of the proposed theories. Observations used to study regions of young massive star formation and properties of the objects associated with massive star formation are presented in section 2.3. Discussion on the variability of masers is presented in section 2.4.

2.2 Evolutionary Stages of High Mass Star Formation

The formation of high mass stars involves multi-stage processes. Some of these stages are not well understood, both theoretically and observationally. Different authors have different views of what actually happens during the formation of high mass stars. The discussion presented here is based on simulations done by Shu et al. (1987).

The standard theory of star formation is that stars form from the gravitational collapse of molecular clump cores within giant molecular clouds (GMC). These GMCs, with sizes from 20 – 100 pc, masses ranging between 10^4 and 10^6 $M_\odot$ and densities between 50 and 100 cm^{-3} are seen to be concentrated along spiral arms of galaxies (Stark & Lee, 2005). The formation of GMCs is currently not well understood. They may be formed by condensation out of the atomic ISM induced by large scale gravitational instabilities in spiral shocks (Dobbs et al., 2006).

GMCs are supported against their self-gravity by a combination of turbulent motions, magnetic fields, gas pressure, and centrifugal force. However, at some point GMCs become gravitationally unstable. The mechanism responsible for the cloud instability is not well understood. It may involve a break-down of magnetic fields by the process of ambipolar diffusion, decay of turbulence or be induced by external shock waves caused by supernova explosions.

The gravitational instability of the GMCs occurs when such clouds exhibit non-hydrostatic equilibrium. The non-hydrostatic equilibrium of the GMCs follow the criteria of

$$M_{cloud} > M_j \tag{2.1}$$

where M_j is the Jeans mass, the mass of the cloud or of a cloud core.

If M is the mass of the cloud that is in hydrostatic equilibrium, then the balance of the forces between the outward pressure and the inward gravity can be expressed as

$$\frac{dp}{dr} = -\frac{GM}{R^2}\rho \tag{2.2}$$

where p is the pressure, G is the gravitational constant and R is the radius of the cloud. The pressure force, $\frac{dp}{dr}$, can be approximated as $-\frac{P}{R}$ and equation

2.2 can now be written as

$$-\frac{\mathrm{P}}{\mathrm{R}} = -\frac{\mathrm{GM}}{\mathrm{R}^2}\rho \quad (2.3)$$

Assuming that the pressure in the cloud is equivalent to that of an ideal gas, then

$$\mathrm{P} = \frac{\mathrm{R_g}}{\mu}\rho\mathrm{T} \quad (2.4)$$

where $\mathrm{R_g}$ is the universal gas constant. Thus equation 2.3 can then further be written as

$$\frac{\mathrm{R_g}}{\mu\mathrm{R}}\mathrm{T} = \frac{\mathrm{GM}}{\mathrm{R}^2} \quad (2.5)$$

In order to have collapse the gravitational force has to exceed the thermal pressure, that is,

$$\frac{\mathrm{GM}}{\mathrm{R}^2} > \frac{\mathrm{R_g}}{\mu\mathrm{R}}\mathrm{T} \quad (2.6)$$

Equation 2.5 can be rearranged to

$$\mathrm{M} = \frac{\mathrm{R_g}}{\mu\mathrm{G}}\mathrm{RT}. \quad (2.7)$$

Using

$$\mathrm{M} = \frac{4}{3}\pi\mathrm{R}^3\rho \quad (2.8)$$

and rearrange for R

$$\mathrm{R} = (\frac{3}{4\pi})^{\frac{1}{3}}(\frac{\mathrm{M}}{\rho})^{\frac{1}{3}}. \quad (2.9)$$

Substituting for R into equation 2.7

$$\mathrm{M} = \frac{\mathrm{R_g}}{\mu\mathrm{G}}\mathrm{T}(\frac{3}{4\pi})^{\frac{1}{3}}\mathrm{M}^{\frac{1}{3}}\rho^{-\frac{1}{3}} \quad (2.10)$$

rearranging this equation gives

$$\mathrm{M}^2 = (\frac{\mathrm{R_g}}{\mu\mathrm{G}})^3\mathrm{T}^3(\frac{3}{4\pi})\rho^{-1} \quad (2.11)$$

which simplifies to

$$\mathrm{M} = (\frac{3}{4\pi})^{\frac{1}{2}}(\frac{\mathrm{R_g}}{\mu\mathrm{G}})^{\frac{3}{2}}\mathrm{T}^{\frac{3}{2}}\rho^{-\frac{1}{2}} \quad (2.12)$$

Let

$$M \approx M_j \tag{2.13}$$

so that

$$M_j = (\frac{3}{4\pi})^{\frac{1}{2}}(\frac{R_g}{\mu G})^{\frac{3}{2}}T^{\frac{3}{2}}\rho^{-\frac{1}{2}} \tag{2.14}$$

This is the mass a cloud core should have in order to collapse.

Initially the collapsing cores are optically thin. Material may fall freely onto the core. The gravitational energy released is easily radiated away from the core into space and the temperature does not change much. In this phase, the gravitational collapse of the cloud cores is characterised by the free-fall time given by

$$T_{ff} = (\frac{3\pi}{32G\rho})^{\frac{1}{2}} \tag{2.15}$$

Thus an increase of the density within the cores will reduce the free-fall time of the cloud. This implies that the higher the density the faster the cores will collapse to the centre.

As the core continues to collapse, its density increases and the gas heats up. When the density is high enough (e.g $n(H_2) \approx 10^{10}cm^{-3}$) for the core to become optically thick, the gravitational potential energy released is converted into heat energy and no longer radiated away easily. The trapped energy increases the temperature and pressure of the core. The high pressures in the core pushes the infalling matter away from the centre of the core. At the same time the force of gravity also pulls the matter to the centre. As a result the core slowly settles into hydrostatic equilibrium.

The core is still mostly composed of molecular hydrogen. The central density and temperature of the core continue to rise and at about $\rho_c \approx 10^{-7}$ g cm^{-3} and $T_c \approx 2000$ K molecular hydrogen begins to dissociate absorbing energy at the same time. The loss of energy causes the core to become dynamically unstable and collapse again. This time, the collapse is controlled by the Kelvin-Helmholtz time scale given by

$$t_{KH} \approx \frac{GM^2}{2R} \tag{2.16}$$

When the central density and central temperature reaches $\rho_c \approx 10^{-2}$ g cm^{-3} and $T_c \approx 10^4$ K respectively the dissociation of molecular hydrogen stops and a hydrostatic core forms surrounded by an infalling envelope. This hydrostatic core is called a protostar and is ready to enter the accretion phase.

The protostar continues to accrete matter from the infalling envelope. As the material accretes the gravitational potential energy is lost through radiation. The resulting accretion luminosity of the central core is given by

$$L_{acc} = \frac{GM_{*}\dot{M}_{acc}}{R_{*}} \tag{2.17}$$

where M_{*} and R_{*} are the mass and radius of the protostar and

$$\dot{M}_{acc} = \frac{dM_{*}}{dt} \tag{2.18}$$

is the mass accretion rate. Furthermore the infalling matter also loses angular momentum. In this case material first falls onto a disk surrounding the protostar. As matter falls onto the disk, accretion becomes frictional and viscous, forming a net outward path for the transportation of angular momentum. Bipolar outflows and stellar winds formed during the accretion phase also play an important role in carrying away angular momentum. Thus a combination of frictional and viscous accretion, bipolar outflows and stellar winds allows matter to move from the disk to the protostellar core, enabling the core to grow in mass. A summary of the stages of star formation is shown in figure 2.1.

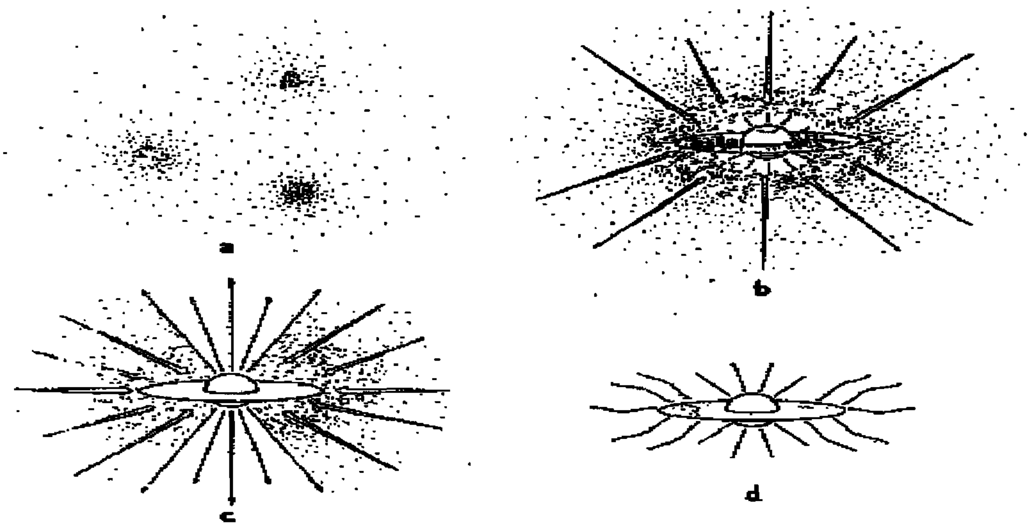

Figure 2.1: Stages of star formation (Shu et al., 1987).(a) Cores form within molecular clouds. (b) Formation of hydrostatic core surrounded by a disk. The arrows show the motion of the infalling material. (c) Bipolar outflow production. The thick arrows show the motion of the infalling material and thin arrows show the direction of the outflow. (d) Newly formed star surrounded by a circumstellar disk.

An increase in the mass of the protostar due to accretion causes the temperature to rise. Once the temperature reaches 10^6 K nuclear reactions begin. The first reaction is deuterium burning. Further evolution of the protostar now depends on its mass. Low mass stars ($M_{star} \leq 7\ M_{\odot}$) undergo a convective phase (pre-main sequence). As the central temperature continues to rise, the opacity of the protostar decreases. At a temperature of about 10^7 K hydrogen burning takes over allowing the protostar to enter the main sequence life-stage.

Stars with mass $M_{star} \geq 8\ M_{\odot}$ are also thought to form through accretion process (Yorke, 2004). However, there is still a lot of debate about its applicability. First, high mass stars have smaller Kelvin-Helmholtz time scales. So they undergo a short accretion phase and hence miss the pre-main sequence stage. As a consequence such stars reach the main sequence and begin nuclear fusion while still accreting matter (Yorke, 2004). Their mass accretion rates range between $10^{-5} - 10^{-3}\ M_{\odot}\ yr^{-1}$ (Maeder & Behrend, 2002). The ongoing nuclear reactions produce a large amount of luminosity which is accompanied by radiative pressure forces. These forces could be much greater than the momentum of the infalling material and so they may be able to overcome the gravitational force and hence stop further accretion (Yorke & Kruegel, 1977). Theoretical work by Yorke & Sonnhalter (2002) confirmed the validity of the radiative pressure forces problem. They found that radiative pressure indeed affected the accretion process for masses above 40 $M_{\odot}$.

A number of mechanisms have been put forward to solve this problem. For instance, Yorke & Kruegel (1977) suggested that radiation pressure can be overwhelmed by high densities and ram pressures associated with the infalling material. In their turbulent core model, McKee & Tan (2003) proposed that accretion onto the star can proceed if the mass accretion rate is proportional to the stellar mass. Krumholz et al. (2005) suggested that a bubble wall left by the radiation driven bubble collapse can allow accretion to proceed through an accretion disk. They also argue that the production of outflows and stellar winds can result in cavities which allows much of the radiation to escape without hindering accretion onto the disk.

Observations of high mass stars indicate that most of these stars are found in close binaries (Mason et al., 1996). The formation of close binaries may involve three-body encounters in the centres of clusters (Malmberg et al., 2007). Owing to their larger cross-sections, binaries may be forced to further interact with other stars (low or intermediate mass stars) and cause mergers which result in the formation of high mass stars (Bonnell, 2002). The merger theory requires that the time scales for the collision should be less than the ages of the clusters, the birth place of high mass stars (Bonnell, 2002). Numerical simulations by Bonnell et al. (1998) showed that a possible collisional time scale of $\lesssim 10^5$ yr can be achieved if the stellar density is $\gtrsim 10^8$ star pc^{-3}. Such densities are very high and have not been observed in active clusters of high mass star formation.

Even if these clusters exist as suggested by Bonnell et al. (1998), the result of close encounters is not well understood.

Both the proposed models pose theoretical challenges. First, the current simulations of radiation pressure effects have not been observationally confirmed. Secondly, the merger process requires very high stellar densities. However, it may be possible that the two processes are both involved in the formation of high mass stars. Apart from theoretical problems, studies of high mass star formation are also difficult in terms of observations. Observational difficulties are partly due to the complex nature of the regions in which such stars are formed.

2.3 Tracers of Young High Mass Stars

High mass stars form in regions that are much more distant than low mass star forming regions. That is, while the Taurus-Auriga is the nearest region of low mass star formation found at a distance of 140 pc, the nearest region of high-mass star formation, viz the Orion molecular cloud, is found at a distance of 450 pc from the Sun. In addition, the formation of high mass stars takes place in clusters with stellar densities between 10^2 and 10^4 stars pc^{-3}. These clusters may contain multiple groups of stars and the majority of the stars may be found in binaries. Hence the studies of high mass stars demand high spatial resolution. In almost all their stages, high mass stars evolve much faster than low mass stars (see figure 2.2 for their lifespans) so it is hard to catch them forming. Furthermore, young high mass stars (protostars) are deeply obscured by dust and gas. Therefore they are non-detectable at optical and near infrared wavelengths.

The characteristics of high mass star forming regions, i.e scarce, changing rapidly, at large distances, and in clusters, restrict the study of the formation process of such stars. Hence much of what is known is obtained from the observations of the surrounding environment (e.g H II regions, bipolar outflows, hot cores and masers). Characteristics of some of these sources are discussed below.

2.3.1 H II Regions

O- and B-type stars emit a significant amount of UV radiation. The UV radiation ionises the surrounding medium and forms an ionisation front which may propagate forming a Strömgren sphere of ionised hydrogen, known as an H II region. The evolution of H II regions follows the following sequence:

hypercompact H II region ⟶ ultracompact H II region ⟶ compact H II region ⟶ extended H II region.

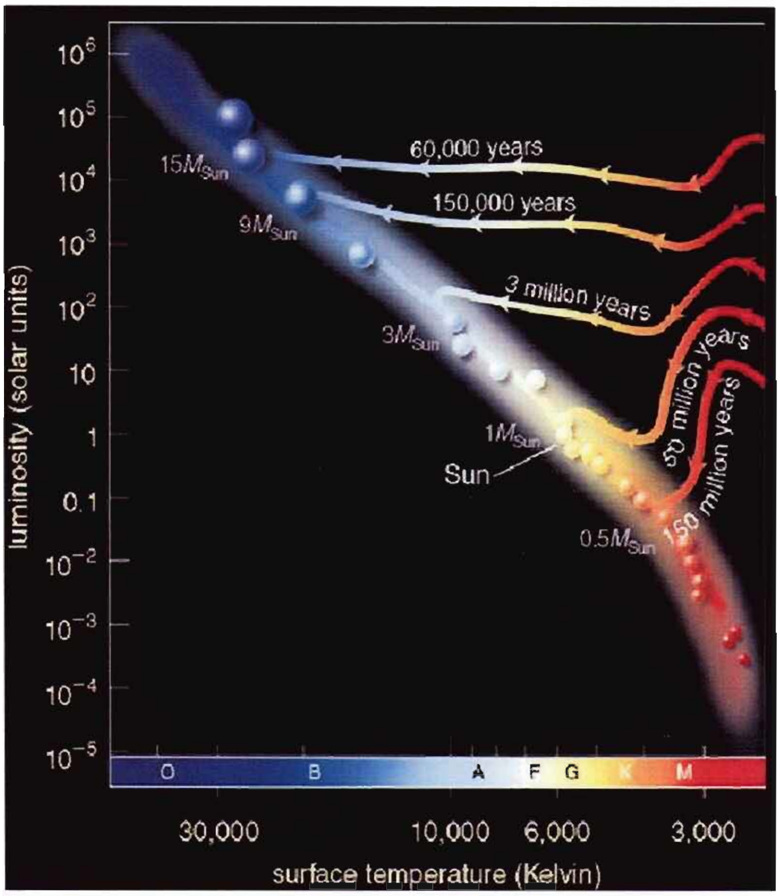

Figure 2.2: Stellar lifetimes. (http://astro.physics.uiowa.edu/~kaaret/genastro07s/L08_starform2.ppt)

Hypercompact H II regions are the earliest observable stage of H II region formation and are characterised by sizes of approximately 0.003 pc, density $\geq 10^6$ cm^{-3} and emission measures about $\geq 10^8$ pc cm^{-6}. They are very faint, short-lived and hence not easily detected. Hypercompact H II regions are structured by outflow jets, rotating disks and shocks (Sewilo et al., 2004). These regions may be formed before the accretion process stops.

Expansion of hypercompact H II regions leads to the formation of ultracompact (UC) H II regions. UC H II regions are small (diameter between 0.01 and 0.1 pc), bright with emission measures of $\geq 10^7$ pc cm^{-6} and densities greater than 10^4 cm^{-3}. Interferometric radio continuum observations have shown that

UC H II regions show different characteristic shapes: spherical, cometary, shell-like, bipolar, irregular and unresolved (Churchwell, 2002; De Pree et al., 2005). These morphologies may provide clues about molecular environments harbouring UC H II regions. UC H II regions are found deeply embedded within small, typically $\leq$ 0.5 pc, dense ($> 10^5$ cm^{-3}) and hot (100-200 K) molecular cloud cores. Recombination lines and free-free continuum emission emitted by UC H II regions provide information about the kinematics of the ionised gas. Single dish observations of NH_3(4,4) and (5,5) towards UC H II regions have shown that most of the UC H II regions are associated with molecular gas as evidenced by the high detection rates of excited NH_3 (Cesaroni et al., 1992). In addition, UC H II regions are often associated with hydroxyl, water and methanol masers (Walsh et al., 1998).

2.3.2 Interstellar Masers

Interstellar masers (Microwave Amplification by the Stimulated Emission of Radiation) are regions of gas where incoming radiation is amplified by molecules near the newly formed stars. The formation of masers requires that the population inversion condition be satisfied. Population inversion occurs when more molecules are in the higher energy levels than are in the lower energy levels. For this condition to hold there must be a means of pumping the molecules to the higher energy state. Such processes may involve collisions between the molecules of a gas and other particles, or light absorption which may result from the interaction of a photon with a molecule. When a molecule in the inverted population is exposed to radiation it may be de-excited to the lower state, emitting a photon with an energy equal to the energy difference between the higher and lower levels. Maser emission may be detected mostly in regions where there is a large column density of molecules and a long path length with velocity coherence along the line of sight. The detected radiation appears in the form of strong, narrow spectral lines. The non-thermal nature of maser emission is apparent from the narrowness of these spectral lines and high brightness temperatures. A number of molecular species have been found to show maser emission, some of which are discussed below.

Hydroxyl Masers

Hydroxyl masers were the first masers to be discovered in interstellar space (Weaver et al., 1965). These masers are observed in regions of star formation, the envelopes of evolved stars, as well as in external galaxies. Hydroxyl masers are often associated with compact H II regions (Habing & Israel, 1979), bipolar outflows (Brebner et al., 1987) and are sometimes observed close to UC H II regions (Forster & Caswell, 2000). These masers are believed to be radiatively pumped by infrared radiation(Cragg et al., 2002). Hydroxyl masers are mostly detected in four transitions, namely: 1665 MHz, 1667 MHz (known as main lines), 1612 MHz and 1720 MHz (known as satellite lines). The main lines are the most commonly observed with 1665 MHz being stronger than the 1667 MHz counterpart. However, the two transitions are closely associated. Caswell (1998) used the Australia Telescope Compact Array to observe about 200 1665 MHz hydroxyl masers. Their results showed that most of the maser sites with 1665 MHz also had 1667 MHz counterparts.

Water Masers

Water masers were the second masers species to be discovered following hydroxyl masers. These masers were detected at 22 GHz towards regions of star formation by Cheung et al. (1969). Many other transitions were later detected in both star-forming regions and the envelopes of late-type stars (Menten et al., 1990; Melnick et al., 1993). Water masers are often associated with high velocity outflows emanating from young stellar objects (Elitzur, 1992). Such masers may be collisionally pumped (Anderson & Watson, 1990). The water masers associated with star forming regions exhibiting maser emission are characterised by low velocity features with strong flux densities and high velocity features with weak flux densities (Fiebig et al., 1996). Such behaviour may be explained in terms of collisional pumping mechanism of water masers (Gwinn, 1994). Numerous water masers are seen to be associated with regions of high mass star formation. De Buizer et al. (2005b) reported over 75% detection rate of water masers towards such regions. The same authors found that most water masers are also associated with mid-infrared sources, evidenced by a median separation of ~8700 AU between the mid-infrared sources and the centres of water masers.

Methanol Masers

The first discovery of methanol masers was made by Barrett et al. (1971). These masers were detected at 25 GHz in the Orion A molecular cloud. Almost 16 years later another discovery was made by Batrla et al. (1987) at 12.2 GHz which was later followed by detections at 6.7 GHz (Menten, 1991b). Owing to the fact that the 6.7 GHz and 12.2 GHz masers were seen in the same regions of high mass star formation, but not coincident with 25 GHz masers, Menten (1991a) divided these masers into two classes. The classification of methanol masers also depended on their association with infrared sources and pumping mechanisms.

Class I methanol masers include those detected in the 25-, 36-, 44-, 84-, 95- and 146-GHz transitions. They are found in both regions of low and high mass star formation. Class I methanol masers are collisionally pumped (Sobolev, 1993). The masers show a single feature with narrow line widths (<0.03 km s^{-1}) in their spectrum (Voronkov et al., 2006). Class I methanol masers appear as spots which are often correlated with shocked gas traced by H_2 emission (Voronkov et al., 2006). This supports the idea suggested earlier on by Menten (1996) that class I methanol masers are often associated with outflows.

Class II methanol masers show emission at 6.7-, 12.2-, 19-, 23-, 28-, 37.7-, 38-, 85.5-, 86-, 107-, 108.8-, and 156-GHz. These masers are often seen projected onto UC H II regions. However, they may also be found offset from UC H II regions (Walsh et al., 1997). Walsh et al. (1998) speculated that class II methanol masers are associated with dense massive molecular cores that have not yet produced detectable UC H II regions. They argue that these masers are then destroyed as the UC H II regions evolve. Observations by Codella & Moscadelli (2000) and Beuther et al. (2002) strongly support the conclusion that class II methanol masers are associated only with regions of high mass star formation. Thus they provide a unique way of identifying and studying the kinematics of such regions.

Most of class II methanol maser sources show emission only at 6.7 GHz and 12.2 GHz. These two transitions are the most widespread, brightest and are closely associated. However, the 6.7 GHz methanol masers are very luminous and normally more intense than their 12.2 GHz counterparts.

The high brightness temperatures of class II methanol masers have a major implication for their excitation mechanisms. It has been suggested that class II methanol masers may be radiatively pumped through torsionally excited states (Sobolev & Deguchi, 1994). The calculations showed that the radiative transitions between the second torsionally excited states and levels of the ground states are greater when the radiative temperature is $\geq$ 150 K. At these temperatures, the masers are pumped by infrared radiation emanating from the dust in the vicinity of UC H II regions (Wink et al., 1994). Current suggestions are that these masers are radiatively pumped (Cragg et al., 2005).

Class II methanol masers in regions of high mass star formation can be searched for using two methods. These methods are classified as targeted and unbiased, and they vary with respect to spatial coverage as well as detection sensitivity statistics. Biased methods, however, fail to detect the presence of masers in untargeted and unexpected areas. On the other hand, unbiased surveying methods cover a wider region and are only limited by the sensitivity of the observations.

The searches for methanol masers using biased surveying methods were performed either by selecting sources associated with other maser species (MacLeod et al., 1992; Gaylard et al., 1994; Caswell et al., 1995c) or by selecting IR sources having IR colours of UC H II regions (MacLeod et al., 1993; Schutte et al., 1993; Walsh et al., 1997; MacLeod et al., 1998). The results showed a close association between 6.7 GHz and 12.2 GHz masers. For example, there was a 100% detection rate of 6.7 GHz masers towards 12.2 GHz masers (MacLeod et al., 1992). A number of unbiased surveys were also carried out (e.g, Caswell (1996a,b); Ellingsen et al. (1996b); Szymczak et al. (2002)). Observational results of these surveys have indicated that not all methanol masers are associated with IRAS point sources.

Class II methanol masers are often seen in close association with hydroxyl masers e.g Gaylard & MacLeod (1993), Caswell et al. (1995d) and Caswell (1997). Position measurements of methanol and hydroxyl masers indicate that the two masers are largely coextensive, with coincidence of about one arcsecond (Caswell, 1997). The high resolution detections of the two maser species from the same star-forming regions may imply that masers emanate from the same volume of gas surrounding recently formed stars (Caswell, 1996b). In most cases the associated maser species show similar velocity distributions (Menten et al., 1992; Etoka et al., 2005; Harvey-Smith & Cohen, 2006). On small scales methanol and hydroxyl masers are anticorrelated (Menten et al., 1992). This is evidenced by the discovery of extended filamentary structure perpendicular to the UC H II region in W3(OH) (Harvey-Smith & Cohen, 2006). Under the following conditions: e.g $T \leq 100$ K and $10^5 \leq n \leq 10^8$ cm^{-3}, the two maser species may be pumped by infrared radiation (Cragg et al., 2002).

The location of Class II methanol masers is still not clearly understood. Class II methanol masers exhibit various morphologies, and sometimes have velocity gradients along them (Norris et al., 1998; Walsh et al., 1998; Minier et al., 2000; Dodson et al., 2004). The arc-like or curved morphologies are thought to be due to inclined disks (Norris et al., 1998). Linear structures are suspected to originate in some fraction of a disk which is seen edge-on around a high mass star (Minier et al., 2000). However, there are other class II methanol masers which do not have these arc-like or linear morphologies and velocity gradients (Norris et al., 1998; Walsh et al., 1998). Possible location of class II methanol masers with arc-like or linear morphologies and velocity gradients along them are discussed below.

Disks

Methanol maser spots are often distributed in lines or arcs with velocity gradients along the axis of such lines, eg Norris et al. (1993). Norris et al. (1993) interpreted this phenomena as evidence of edge-on circumstellar disks around young massive stars. Disks are associated with the accretion process of star formation. Such disks have been observed in a number of young high mass objects, e.g Cesaroni et al. (1999), Beuther et al. (2004b) and Beuther et al. (2005). The edge-on disk model for methanol masers is based on the hypothesis that the maser radiation is only excited in directions along the plane of the disk. Assuming Keplerian rotation, Norris et al. (1998) and Minier et al. (2000) derived the disk radii and enclosed mass of the maser sources showing linear structures. The obtained values ranged between 500 and 2000 AU for the radii and 3 to 100 $M_{\odot}$ for the enclosed masses, both agreeing with theoretical models of accretion disks around massive stars (Lin & Pringle, 1990).

The edge-on disk model was also supported by Minier et al. (2000) but with a different outlook. In their VLBI observations of 14 star-forming regions, 10 were reported to show elongated structures with linear velocity gradients along them. However, the linear structures were too small (radii between 50 and 1300 AU and mass from 1 to 75 $M_{\odot}$) compared with those calculated by Norris et al. (1998). Motivated by these findings the authors suggested that methanol masers could be tracing only part of the edge-on circumstellar disk. Three-dimensional simulations by Durisen et al. (2001) suggested that the persistence of spiral structures accompanied by gravitational instabilities in the outer disks may provide conditions for the methanol maser action.

Recently, Bartkiewicz et al. (2005) found methanol masers distributed in a ring structure around a young embedded high mass star. The authors suggested that these masers arise in a spherical bubble or in a rotating disk seen nearly face-on around a high mass star.

Shocks

The linear structures of methanol masers may also arise from shocks. The shock model was initially proposed by Norris et al. (1993). However, it was found that the model could not produce the velocity structures observed in many maser sources showing linear structures. Arguments by Walsh et al. (1998) are that linear velocity structures are not common features of maser sites. Their surveys showed that only 12 out of 97 methanol maser sites exhibited such linear velocity gradients. Thus they proposed that methanol masers may form behind an expanding shock. The model assumes that the maser spot locations are dense knots of material that have been compressed and accelerated by the passage of the shock. A different view of the shock model was presented by Sobolev & Deguchi (1994) and Sobolev et al. (1997). They proposed that the shock front exists before the ionisation front and creates clumps within the interstellar clouds. Shocks could have the effect of producing more methanol by sublimation off dust grains. Hence methanol masers may be formed by the shock front itself.

Owing to the fact that methanol masers have velocities ranging between 5 and 10 km s^{-1} (Moscadelli et al., 2002), Dodson et al. (2004) suggested that methanol masers may arise in planar shocks with velocity of less than 10 km s^{-1}.

Outflows

Another possible way to explain the methanol maser distribution is through outflows. A number of studies have shown that outflows are common in high mass stars, e.g Shepherd & Churchwell (1996) and Moscadelli et al. (2002) and they indicate the occurrence of an early stage of star formation. Such outflows are associated with H_2 emission from shocks. Kumar et al. (2002) reported a 100% detection of H_2 emission in seven high mass star forming regions showing the existence of outflows. In a sample of 28 sources surveyed by De Buizer (2003), 18 were found to display H_2 emission mostly parallel with the methanol maser distribution. Similar results were also reported by Walsh et al. (2002) and Furuya et al. (2002). Inspired by their findings, De Buizer (2003) suggested that methanol masers are directly associated with outflows.

2.4 Variability of Masers

The variability of masers associated with high mass star forming regions is important in the sense that:
(1) it may help in understanding the changes and physical conditions of such regions,
(2) it helps to study the innermost regions around young massive stars,
(3) it places restrictions on maser pumping mechanisms.

A two year monitoring program of the source S255 showed anticorrelated variability of water masers between velocity components on a time scale of few months (Cesaroni, 1990). Short and long term variability of water masers in W31A and W75S sources was also reported by Lekht et al. (1995). The observations revealed an anticorrelation of fluxes as well as the change of the radial velocity of single components.

Most hydroxyl masers associated with high mass star forming regions show variability on a time scale of between days to years. Clegg & Cordes (1991) observed amplitude fluctuations ranging from 5 to 10 percent over short time scales e.g minutes to hours and between 0 to nearly 100 percent over longer time scales of days to months. These variations were proposed to be due to pulsations of the stellar pumping source. Ramachandran et al. (2006) detected intrinsic variability of hydroxyl masers in the star-forming region W3(OH) on timescale between 15 to 20 minutes.

Methanol masers often show variability on both short and long term. Variability of both 6.7 GHz and 12.2 GHz was detected by Caswell et al. (1995a) on time scales of a month and more. The detected variability was characterised as quasi-periodic. They interpreted the variability as due to the changes in the masing path length. Observations by MacLeod & Gaylard (1996) revealed aperiodic flares in G351.78-0.54 occurring several times per year. In a sample of 54 sources Goedhart et al. (2004) found that some of the sources showed periodic, aperiodic or quasi-periodic variability on a time scale ranging from less than a week to several months.

The G12.89+0.49 star-forming region is one of the 54 sources monitored by Goedhart et al. (2004). In contrast to the other sources this source displayed unusual behaviour. As a result the source G12.89+0.49 was selected for further observations on a daily basis. The next chapter discusses the reasons for re-observations of the G12.89+0.49 star-forming region. It also discusses the G351.42+0.64 star-forming region which is used as a reference source to the G12.89+0.64 observations.

Chapter 3

Source Selection

3.1 Introduction

This chapter discusses why the source G12.89+0.49 was selected for intensive monitoring. The properties of the reference source G351.42+0.64 are also discussed. Furthermore, a wide view of the target source in terms of previous studies undertaken is given.

3.2 Source Selection

The 6.7 GHz methanol masers in the G12.89+0.49 star-forming region were monitored by Goedhart et al. (2004). Figure 3.1 shows the average spectrum at 6.7 GHz obtained from their observations. The resulting time series is shown in Figure 3.2. The peak at $\sim$39 km s^{-1} was reported to show a flickering behaviour on a timescale of 1-2 weeks. This flickering had not been fully sampled by the previous fortnightly monitoring. Errors that may have occurred during the calibration process were ruled out as a possible cause of the flickering as similar flickering behaviour was not seen in any of the other monitored sources. The rest of the peaks were found to exhibit little variability, hence their behaviour was not characterised.

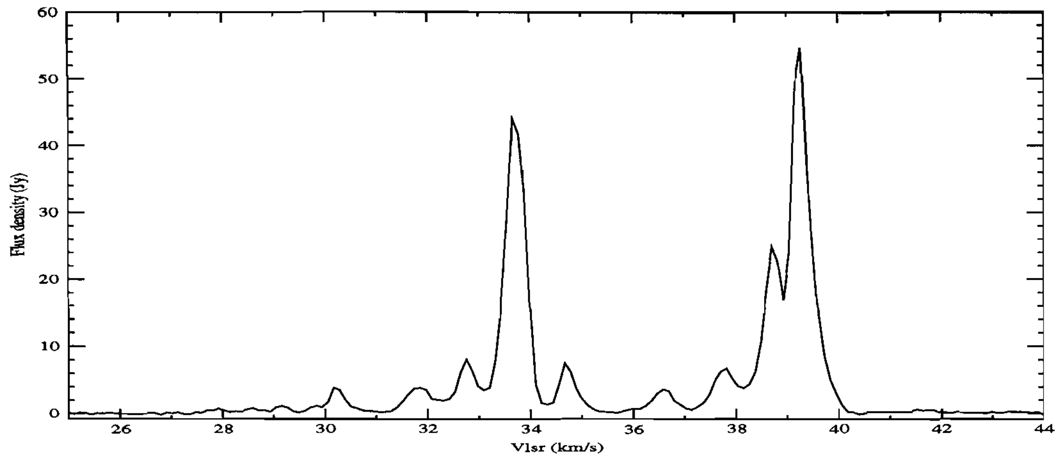

Figure 3.1: The G12.89+0.49 average spectrum at 6.7 GHz masers (Goedhart et al., 2004)

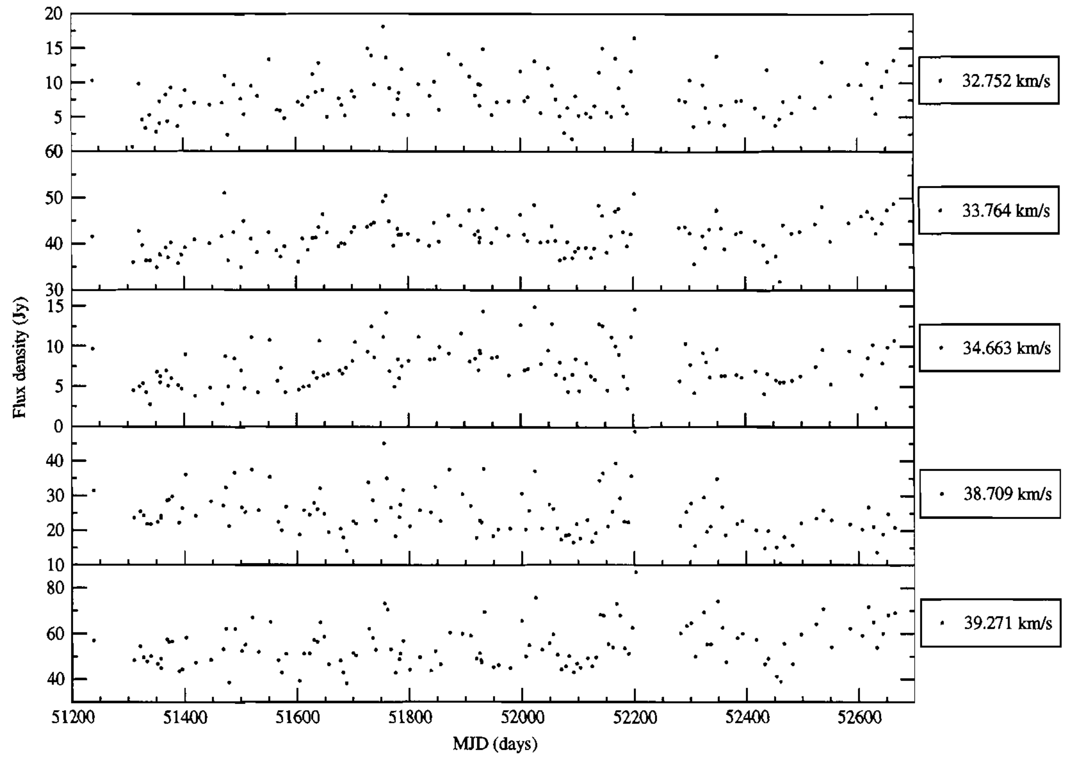

Figure 3.2: The G12.89+0.49 time series at 6.7 GHz (Goedhart et al., 2004)

In addition, the G12.89+0.49 star-forming region also has 1665 MHz hydroxyl masers. These masers are strong enough to be monitored using the 26-m telescope at HartRAO.
The presence of both methanol and hydroxyl masers in the G12.89+0.49 star-forming region makes it an interesting source to study, especially if one is interested in knowing about the characteristics or behaviour of the two masers species and the maser pumping mechanisms.

Motivated by the above mentioned points, daily monitoring of the methanol and hydroxyl masers in the G12.89+0.49 was set up. The main aims were:
(1) to determine the variability behaviour of the source,
(2) to investigate the causative mechanisms of G12.89+0.49 maser variability and
(3) to investigate the relation between G12.89+0.49 methanol and hydroxyl masers.

3.3 Features of G12.89+0.49 Star-Forming Region

The source G12.89+0.49 is also known as IRAS 18089-1732. This area is described as one of the richest regions of high mass star formation in the Galaxy. It is located at a distance of $\sim$ 3.6 kpc from the Sun and has a luminosity of $\sim 3.3\times10^{4.5}$ $L_\odot$ (Sridharan et al., 2002). Based on this luminosity, Purcell et al. (2006) estimated the source to be earlier than a B0 spectral type. A number of studies towards the G12.89+0.49 star-forming region were done at different wavelengths using different tracers and these are discussed in the following sections.

3.3.1 Radio Continuum Emission

Sridharan et al. (2002) imaged free-free and dust continuum emission at 3.6 cm and 1.2 mm wavelengths. The results showed a faint centimetre radio source (0.9 mJy), water and methanol maser emission. The centimetre radio source was reported to be offset from the millimeter emission by 1.1×10^4 AU. The interpretations were that the free-free and dust emission may be arising from the same region. Radio continuum observations using the VLA at 7 mm wavelength have revealed that G12.89+0.49 is a double source (Zapata et al., 2006) (see figure 3.3). The components were found to be separated by 7200 AU, at a distance of 3.6 kpc, along the northeast-southwest direction. Component (a) was reported to be associated with thermal jets or stellar winds and component (b) with dust emission and possibly with an optically thick H II region. Submillimeter observations at 450 μm and 850 μm wavelengths around the 6.7 GHz methanol masers have resulted in a detection of submillimeter continuum emission associated with the 6.7 GHz methanol masers (Walsh et al., 2003).

3.3.2 Molecular Line Radio Emission

Sridharan et al. (2002) performed CO molecular line observations towards the G12.89+0.49 star-forming region using the IRAM 30-m telescope. They detected bipolar outflows evidenced by CO line wings and SiO emission. The authors also reported the detection of thermal emission from CH_3OH and CH_3CN. In a combined observation of SiO(5-4) and $HCOOCH_3$(20-19) molecular lines, Beuther et al. (2004a) reported the detection of a compact submillimeter core with extended halo emission. In the same observations detection of blueshifted and redshifted SiO emission was also reported. The SiO emission is believed to trace outflows from the submillimeter core to the north. In addition, Beuther et al. (2004a) also detected $HCOOCH_3$ emission, a tracer of high-density gas, confined within the central submillimeter core. Assuming that the $HCOOCH_3$ velocity gradient is aligned between the disk plane and the SiO outflow axis, Beuther et al. (2004a) proposed that $HCOOCH_3$ emission may arise from a rotating disk influenced by the SiO outflow. CH_3CN(6-5) and $H^{13}CO^+$ emission were also detected by Purcell et al. (2006). The observation were done using the 92 GHz J=5-4 and 110 GHz J=6-5 transitions of CH_3CN and 86 GHz J=1-0 transition of $H^{13}CO^+$.

3.3.3 Maser Emission

The first detection of methanol masers in the G12.89+0.49 star-forming region were by Kemball et al. (1988) at 12.2 GHz line. In the same year Cohen et al. (1988) discovered the first 1665 MHz hydroxyl masers towards the same region. Three years later the 6.7 GHz methanol masers were detected (Menten, 1991b). Further detections of both the 6.7 GHz and 12.2 GHz methanol masers were made, e.g Caswell et al. (1995c), Sridharan et al. (2002) and Caswell et al. (1995b). The G12.89+0.49 star-forming region also shows water masers, first detected by Jaffe et al. (1981) at 22 GHz. These masers are bright, with their strongest peak at 32 km s^{-1}.

3.4 The Comparison Source G351.42+0.64

The masers associated with the star-forming region G351.42+0.64 were selected as a reference or comparison source for the monitoring of G12.89+0.49. This source is also known as NGC 6334F and is located in the molecular cloud associated with the HII region NGC 6334 (Ellingsen et al., 1996a). G351.42+0.64 shows maser emission from methanol and hydroxyl molecules. Figure 3.4 shows the location of both methanol and hydroxyl masers in G351.42+0.64.

Previous observations were done on G351.42+0.64 to study the variability of 6.7 GHz methanol masers (Goedhart et al., 2004). Figure 3.5 shows the average spectrum from these observations. The variability detected from the strongest methanol maser peaks in G351.42+0.64 are shown in time series of Figure 3.6.

The 12.2 GHz methanol masers in the G351.42+0.64 were also monitored by Gaylard, M. (unpublished results). The resulting average spectrum is shown in Figure 3.7. The three strong peaks of the 12.2 GHz methanol masers also show variability with different amplitudes as shown in Figure 3.8.

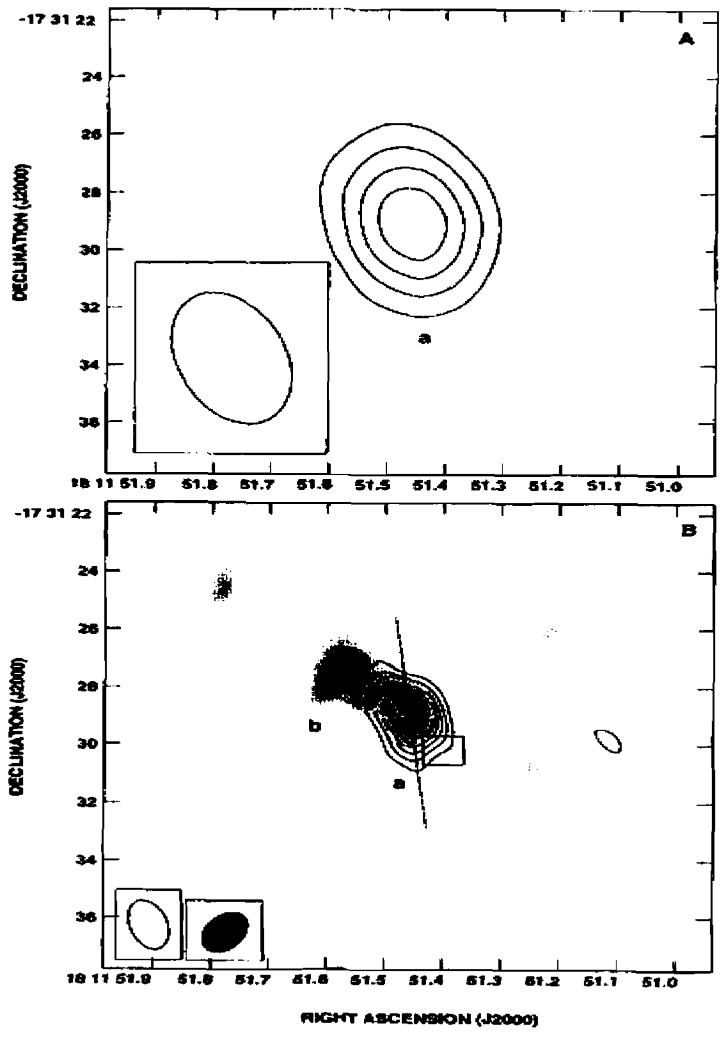

Figure 3.3: VLA images showing the components of the G12.89+0.49 star-forming region (Zapata et al., 2006). The upper figure shows the 3.6 cm emission and the lower one shows the 1.3 cm (contours) continuum emission and 7 mm (gray scale) continuum emission. The square indicates the position of methanol masers (Walsh et al., 1998).

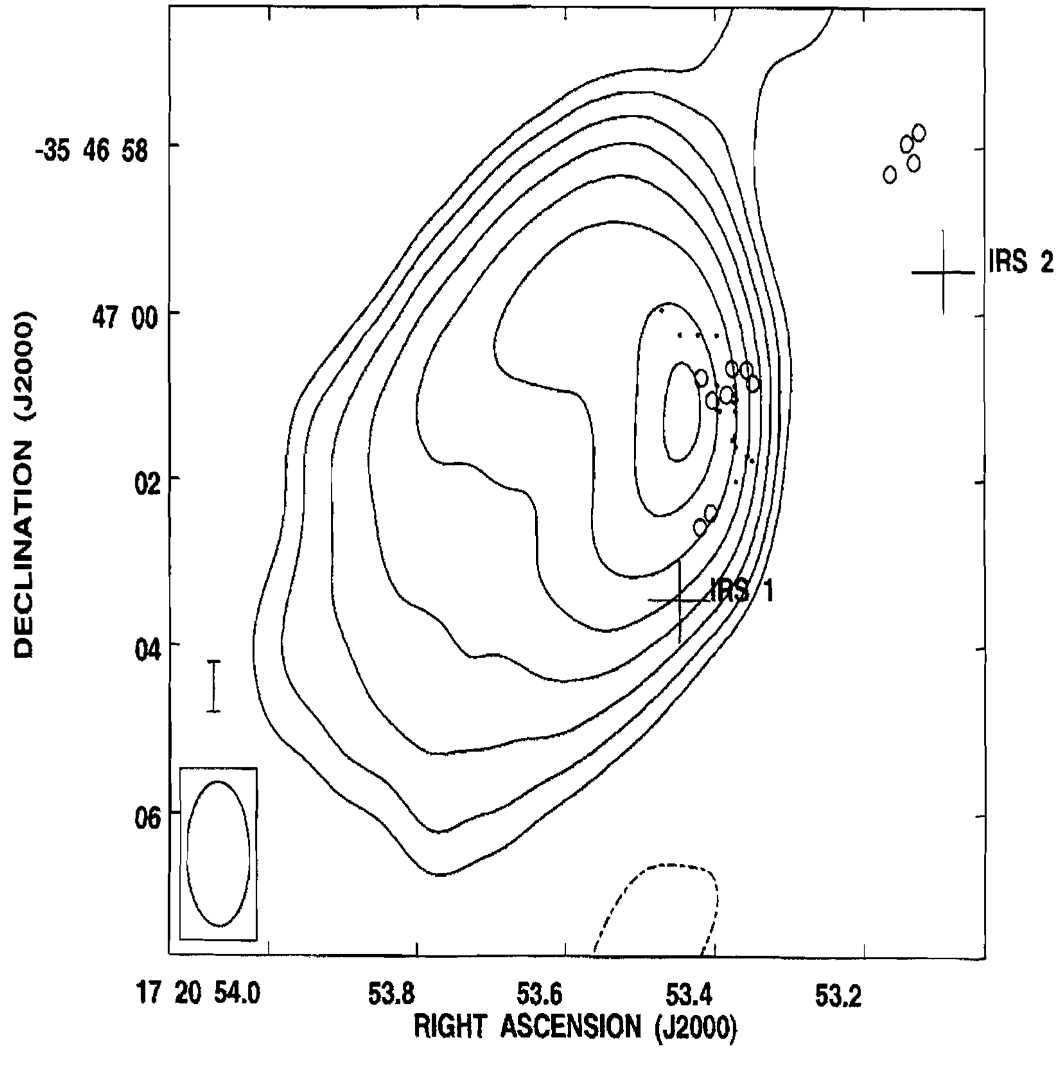

Figure 3.4: Radio continuum image of G351.42+0.64 star-forming region. Methanol maser sites are indicated by the open circles and hydroxyl masers are indicated by dots (Ellingsen et al., 1996a)

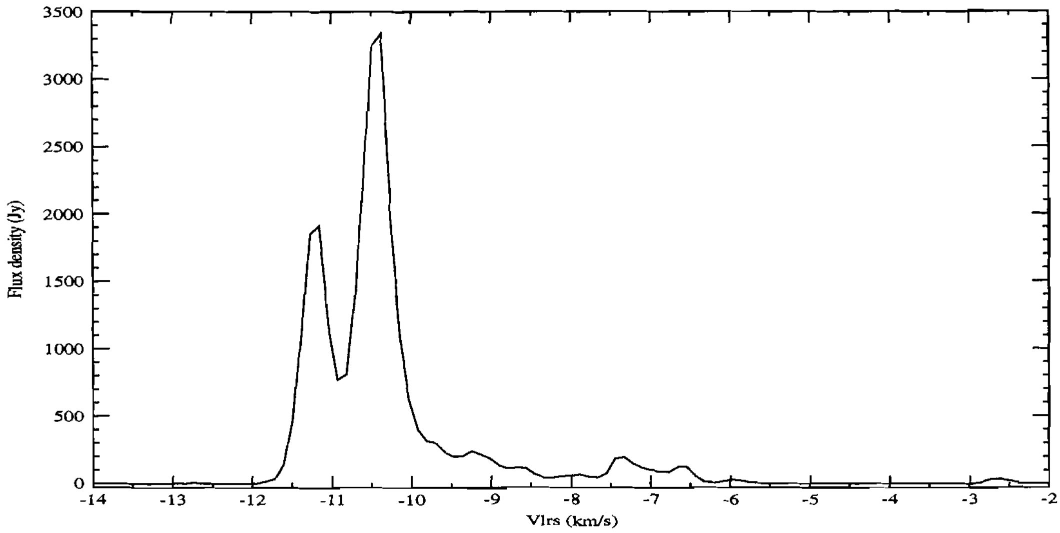

Figure 3.5: The G351.42+0.64 methanol maser average spectrum at 6.7 GHz (Goedhart et al., 2004)

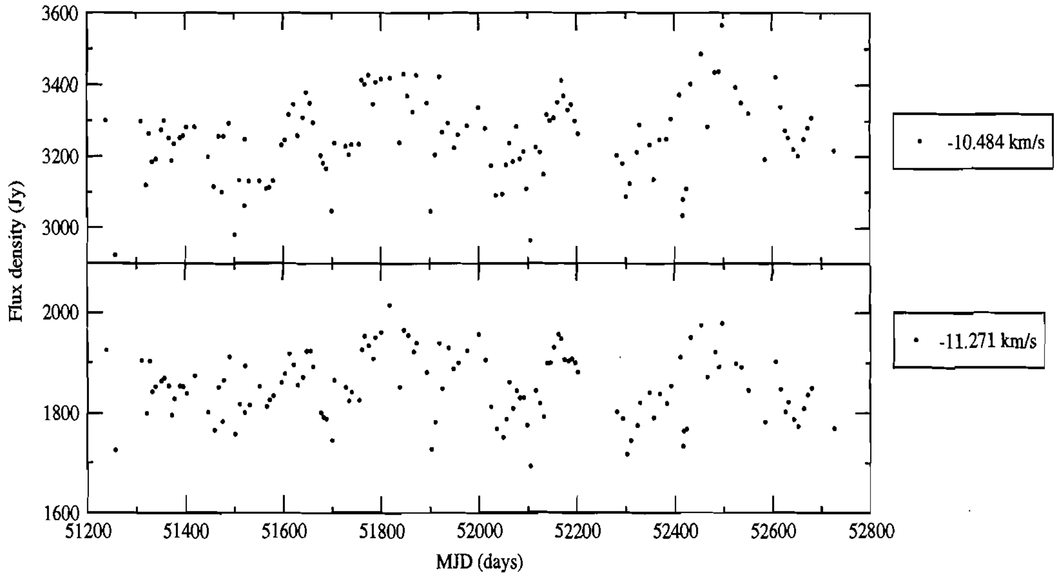

Figure 3.6: The G351.42+0.64 methanol masers time series at 6.7 GHz (Goedhart et al., 2004)

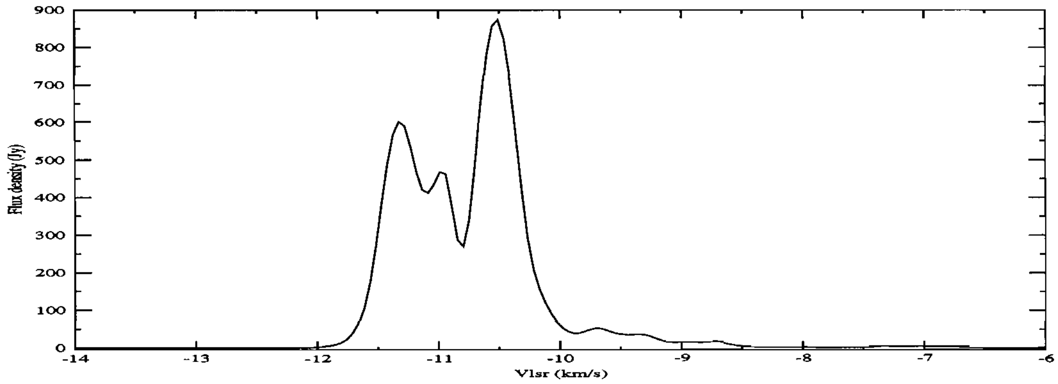

Figure 3.7: The G351.42+0.64 methanol masers average spectrum at 12.2 GHz (Gaylard, M., private communication)

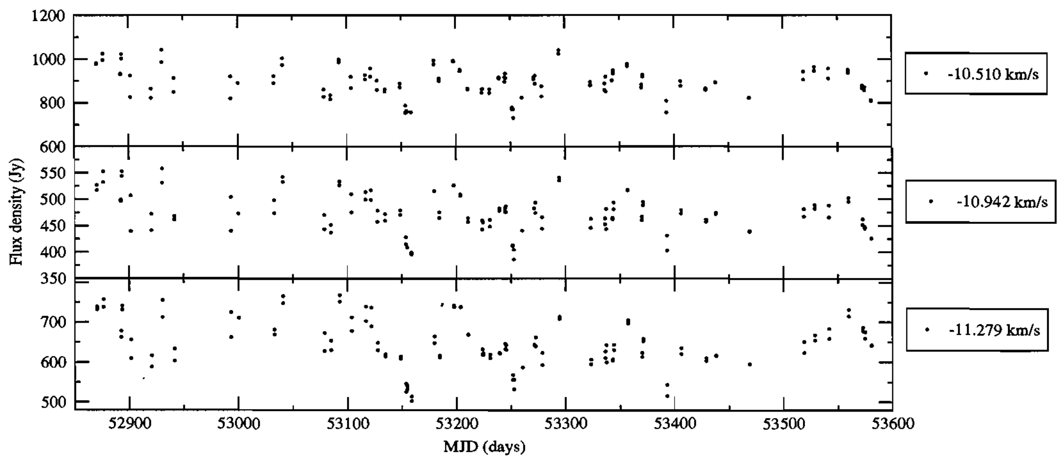

Figure 3.8: The G351.42+0.64 methanol masers time series at 12.2 GHz (Gaylard. M., private communication)

G351.42+0.64 shows small variability in the 6.7 GHz and 12.2 GHz methanol masers. However, this does not affect its use as a reference source since it is used to check for systematic calibration errors. These instrumental errors would be detected if G351.42+0.64 shows the same behaviour as the G12.89+0.49 in these observations. The 12.2 GHz methanol masers in G351.42+0.64 show three strong peaks which also seem to exhibit variability. These three peaks may provide an intensive cross-check of any instrumental errors that may occur during the monitoring of G12.89+0.49.

The observations of both G12.89+0.49 and G351.42+0.64 along with the data reductions are discussed in the next chapter. The chapter also includes the observations of the radio continuum sources used for calibration processes.

Chapter 4

Observations and Data Reduction

4.1 Introduction

The observations undertaken of the target source G12.89+0.49 and the reference source G351.42+0.64 in the three maser transitions are discussed. Calibration errors in single dish observations can be created by bad pointing, focus and changes in the dish surface. In order to account for these errors bright radio continuum sources such as 3C123, Hydra A, and Virgo A were observed at 1666 MHz, 6.7 GHz and 12.2 GHz. Virgo A is partly resolved at 12.2 GHz. Further discussion on the radio continuum observations is presented below in section 4.2 along with the observations of G12.89+0.49 and G351.42+0.64. The data reduction for both spectral line and radio continuum are discussed in section 4.3.

4.2 Observations

The observations were made using the 26-m telescope at HartRAO. These observations started in September 2005 and the data for about a ten month period up to August 2006 have been reduced and are presented here. Methanol masers were observed at 6.7 GHz and 12.2 GHz and hydroxyl masers at 1665 MHz. The reference source G351.42+0.64 was also monitored at the same frequencies. Spectra of both G12.89+0.49 and G351.42+0.64 were taken in left and right circular polarisations. The integration times per observation for the two sources are given in table 4.1. In order to correct the bandpass, pairs of spectra were taken in frequency-switching mode and these pairs were later combined. Table 4.2 gives a summary of the observational parameters for both G12.89+0.49 and G351.42+0.64. For methanol masers in both G12.89+0.49 and G351.42+0.64, pointing corrections were done by offsetting the observations to the half power points of the beam to the north, south, east and west of the source position. The pointing errors at 1665 MHz are negligible because of the large beam.

Table 4.1: Integration time (s) per observation

Line rest frequency (MHz)	6668.518	12178.593	1665.40184
G12.89+0.49	450	450	360
G351.42+0.64	120	180	360

Table 4.2: Spectral line observing parameters

Line rest frequency (MHz)	6668.518	12178.593	1665.40184
Spectrometer channel/polarisation	1024	1024	1024
Spectrometer bandwidth (MHz)	1	2	0.25
Frequency-switching offset (MHz)	0.5	1	0.125
Half power beamwidth (°)	0.116	0.057	0.494
Polarisation	LCP+RCP	LCP+RCP	LCP+RCP

For both G12.89+0.49 and G351.42+0.64, in all maser transitions, a first order polynomial fit was done to the emission free region of the LCP and RCP spectra to measure the rms noise. A typical polynomial fit to the spectra for the two sources are shown in figures 4.1 and 4.2. The percentage error for each spectrum in the LCP and RCP data were estimated from system temperature and system temperature error. Tables 4.3 and 4.4 list the measured rms noise and the percentage error for a typical LCP and RCP spectrum in the three maser transitions for G12.89+0.49 and G351.42+0.64 repectively.

Table 4.3: Typical uncertainty for a particular day in the spectral calibration of G12.89+0.49

Frequency	rms noise (Jy)	Tsys (K)	dTsys (K)	% error
1.665 GHz LCP	0.685	49.046	0.903	1.84
1.665 GHz RCP	0.736	68.760	2.020	2.93
6.7 GHz LCP	0.808	62.156	0.652	1.05
6.7 GHz RCP	0.882	65.609	0.617	0.94
12.2 GHz LCP	0.919	88.244	0.326	0.37
12.2 GHz RCP	0.879	88.112	0.375	0.43

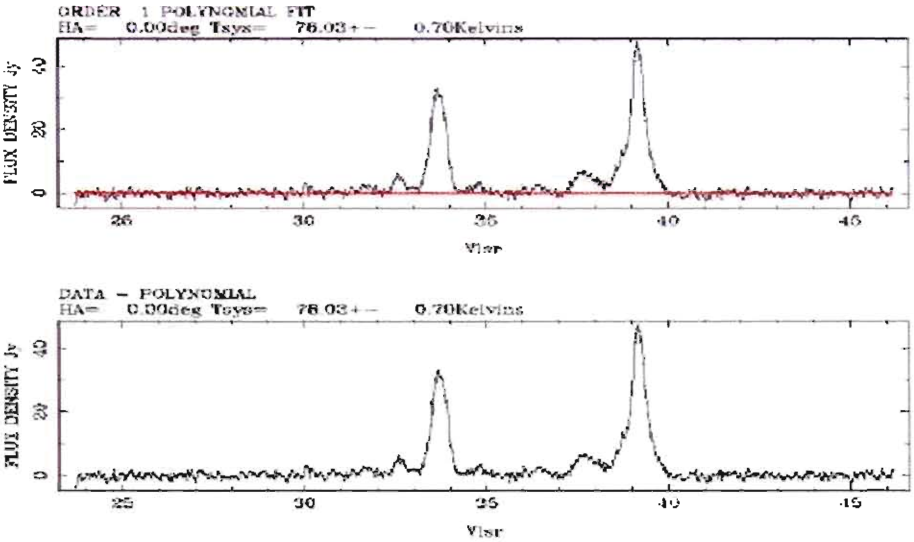

Figure 4.1: The G12.89+0.49 polynomial fit spectrum at 6.7 GHz

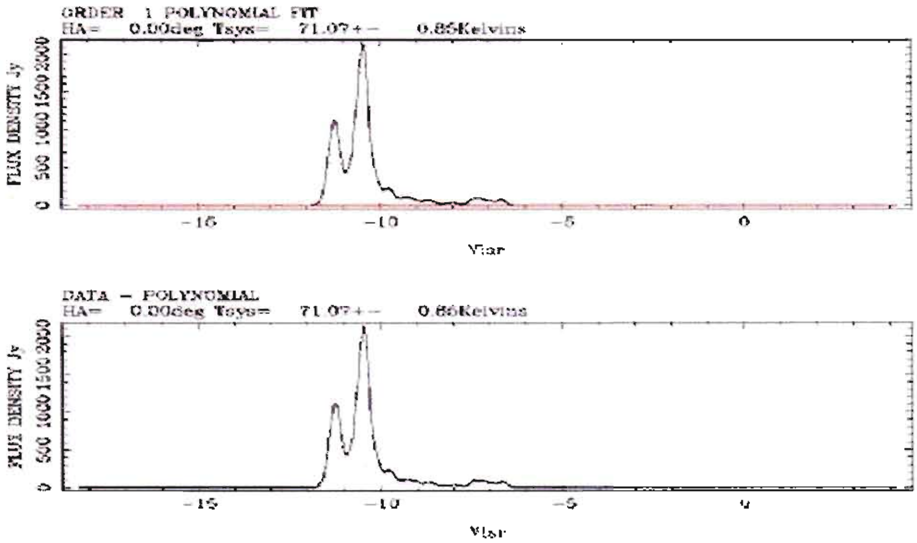

Figure 4.2: The G351.42+0.64 polynomial fit spectrum at 6.7 GHz

Table 4.4: Typical uncertainty for a particular day in the spectral calibration of G351.42+0.64

Frequency	rms noise (Jy)	Tsys (K)	dTsys (K)	% error
1.665 GHz LCP	2.504	68.436	1.646	2.40
1.665 GHz RCP	3.628	92.193	3.893	4.22
6.7 GHz LCP	0.939	73.832	0.923	1.25
6.7 GHz RCP	0.970	74.801	0.686	0.91
12.2 GHz LCP	1.062	91.995	0.343	0.37
12.2 GHz RCP	1.133	91.143	0.382	0.41

The continuum calibrators were also observed daily at left and right circular polarisations. Table 4.5 lists the sources observed at 1666 MHz, 6.7 GHz and 12.2 GHz with their flux densities. Drift scans were carried out at half-power points north and south and on-source in order to correct for pointing errors.

Table 4.5: Calibrators and their flux densities, from Ott et al. (1994)

Source	Frequency (MHz)	Flux density (Jy)
3C123	6668.518	11.76
Hydra A	6668.518	9.99
Virgo A	6668.518	58.71
3C123	12178.593	6.25
Hydra A	12178.593	5.73
Virgo A	12178.593	35.72
Hydra A	1666	36.45

4.3 Data Reduction

The spectral line data in the three observed transitions were reduced using HartRAO's standard procedure 'LINES'. The raw spectral line data included four spectra centered at half-power north, south east and west. Beam offset errors were corrected by combining the intensities from the half-power north, south, east and west points of the beam and on-source for each scan. The band-pass was converted by combining pairs of frequency-shifted on-source spectra.

The radio continuum data were also reduced with 'LINES'. A Gaussian first order polynomial fit was made on each drift scan to flatten the baseline followed by a second order on the top quarter of the beam. The point source sensitivity (PSS) for each scan was calculated from the on-source antenna temperature converted for pointing errors by means of drift scans through the north and south half power points of the beam.

Figures 4.3, 4.4 and 4.5 show the time series for the radio continuum calibrators at 6.7 GHz, 12.2 GHz and 1666 MHz. Investigation of the three time series suggests that 3C123 show less variations in both 6.7 GHz and 12.2 GHz. The PSS derived from this source was therefore adopted.

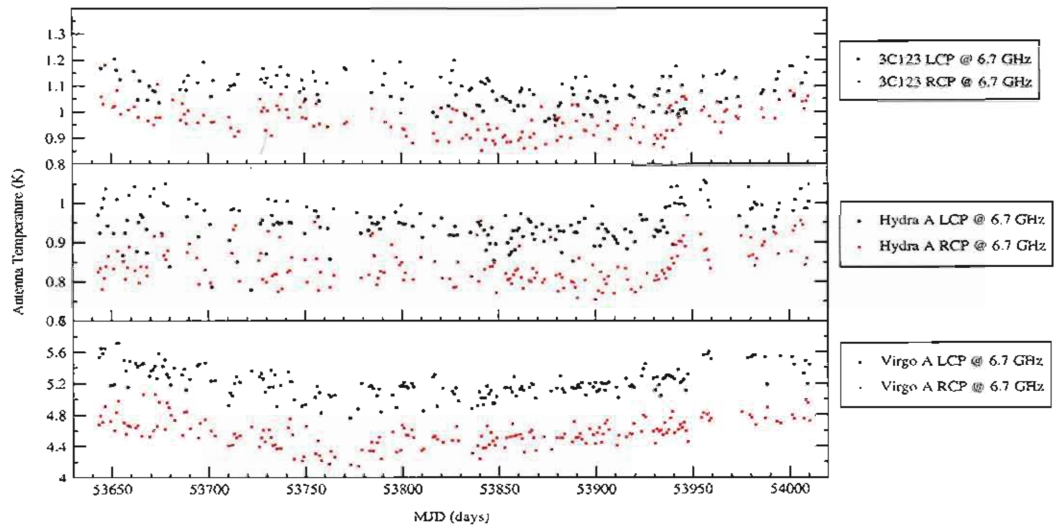

Figure 4.3: Time series for the calibrators at 6.7 GHz

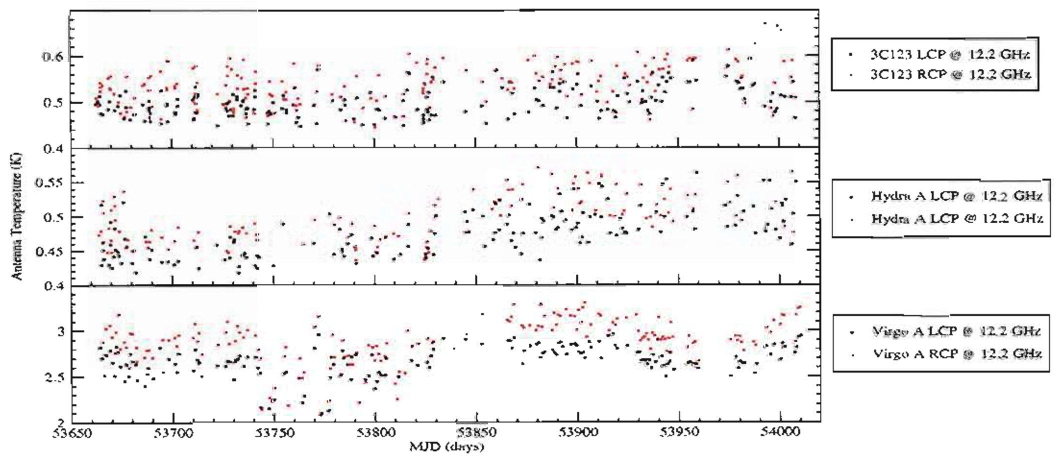

Figure 4.4: Time series for the calibrators at 12.2 GHz

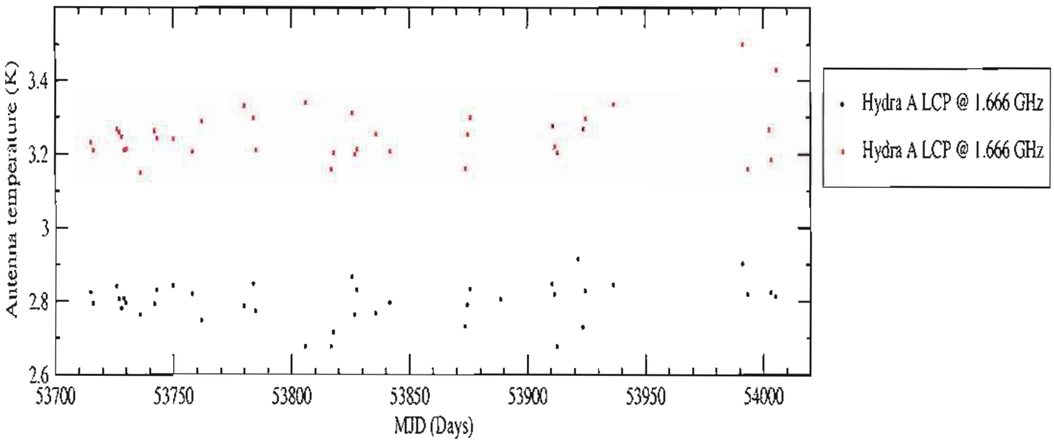

Figure 4.5: Time series for the calibrators at 1666 MHz

The results from the monitoring of G351.42+0.64 and G12.89+0.49 sources at 1665 MHz, 6.7 GHz and 12.2 GHz masers are presented in the next chapter.

Chapter 5

Results and Data Analysis

5.1 Introduction

This chapter presents the spectra and time series results obtained from the daily monitoring observations. The methods used to analyse the data are discussed and the results from these analysis methods are presented.

5.2 Results

Methanol masers are generally unpolarised, so the LCP and RCP spectra were added together. The time series of the total intensity extracted from the spectra of methanol masers at 6.7 GHz and 12.2 GHz and the hydroxyl masers at 1665 MHz are presented.

5.2.1 G351.4+0.64

Methanol Masers at 6.7 GHz

The left panel of Figure 5.1 shows the average spectrum of 6.7 GHz methanol masers. The spectrum shows two strong peaks at -10.42 km s^{-1} and -11.25 km s^{-1}. The corresponding time series are shown on the right panel of the same figure. Both velocity features show significant variations with amplitudes between 1900 Jy and 2200 Jy for the strongest maser peak.

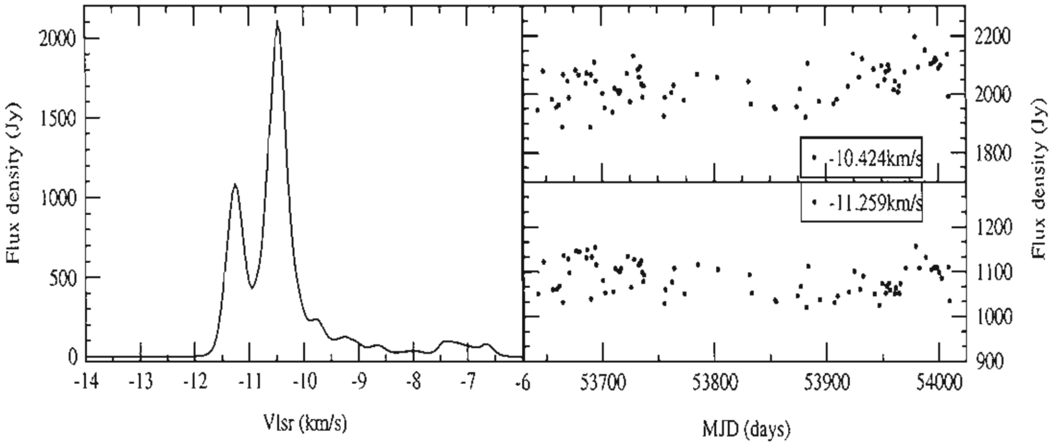

Figure 5.1: The averaged 6.7 GHz methanol maser spectrum and time series for G351.4+0.64

Methanol Masers at 12.2 GHz

The average spectrum for the 12.2 GHz methanol masers in G351.42+0.64 is shown in the left panel of Figure 5.2. The features at -10.46 km s^{-1} and -11.32 km s^{-1} correspond with the two features at 6.7 GHz. The time series of the three features are shown on the right hand side of Figure 5.2. All the three peaks show variability with different amplitudes.

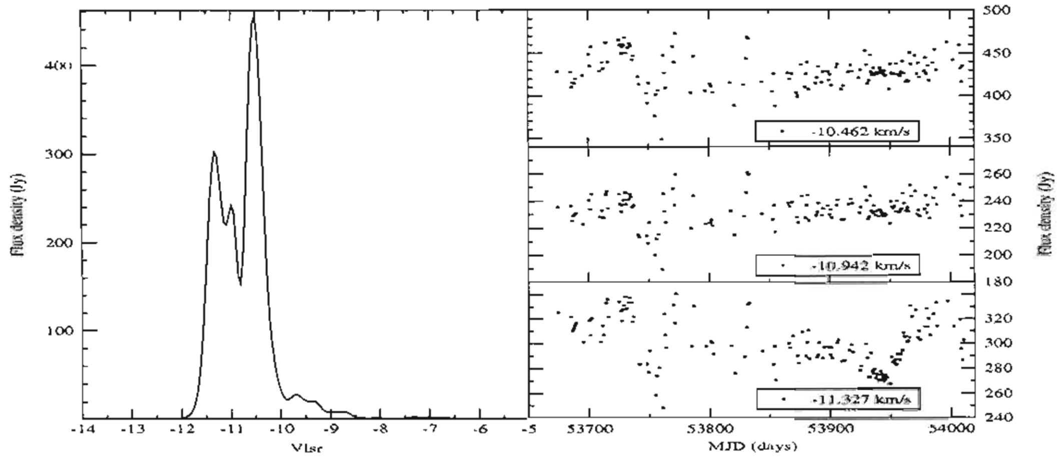

Figure 5.2: The G351.4+0.64 methanol maser average spectrum and time series at 12.2 GHz

Hydroxyl Masers at 1665 MHz

Figure 5.3 shows the LCP and RCP spectra of 1665 MHz hydroxyl masers. The two polarisations are markedly different. The LCP spectrum is composed of one strong and narrow peak with high amplitude and two weak peaks. The spectrum also shows absorption at ~6 km s^{-1} and a weak one at -4 km s^{-1}. The RCP spectrum shows several peaks, the strongest and narrowest being at -11.83 km s^{-1}. The spectrum also shows two absorption lines at ~-4 km s^{-1} and ~6 km s^{-1} corresponding to the LCP absorption line counterparts. The time series for the selected velocity features for both LCP and RCP data are shown in figure 5.4. Both the LCP and RCP time series show no significant variations with respect to time except the peak at -10 km s^{-1}.

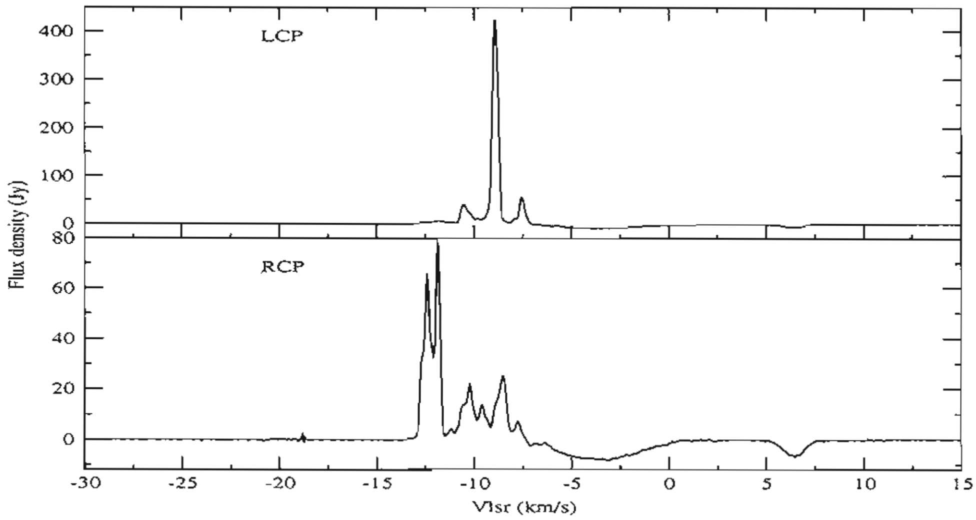

Figure 5.3: The G351.4+0.64 hydroxyl maser spectra at 1665 MHz. Top panel is the LCP average spectrum and bottom one represents the RCP average spectrum

5.2.2 G12.89+0.49

6.7 GHz Methanol Masers

Figure 5.5 shows the averaged 6.7 GHz methanol maser spectrum for the observations from this project overlaid by the previous average spectrum from Goedhart et al. (2004) observations. The masers show strong features at velocity channels of 33.67 km s^{-1} and 39.17 km s^{-1}. Comparison of the velocity features obtained in the present observations with that of Goedhart et al.

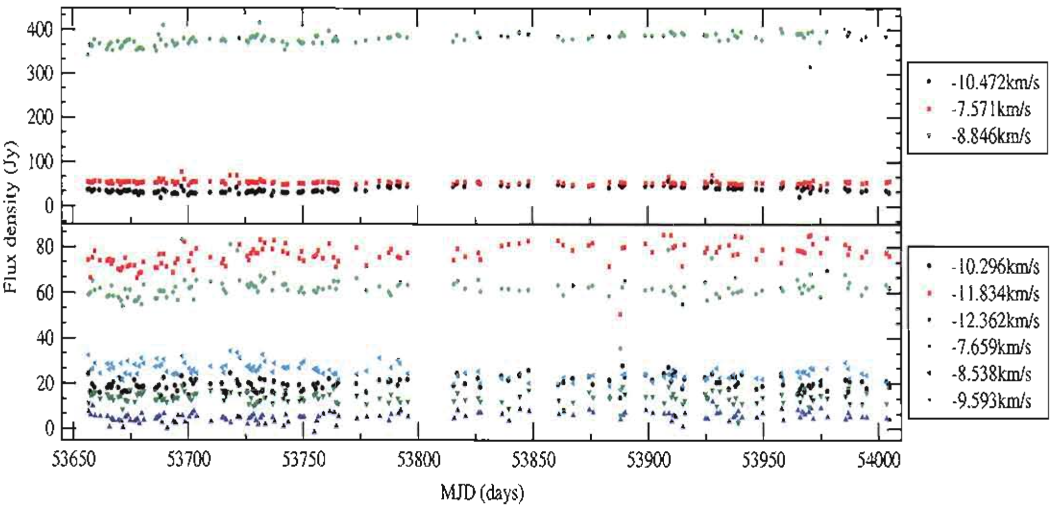

Figure 5.4: The G351.4+0.64 hydroxyl maser time series at 1665 MHz. Top panel shows the time series for LCP and bottom panel shows the time series for RCP

(2004) shows that the average flux density has decreased in all the features. Due to the different spectrometer and software used for the two observations there is a shift of one velocity channel. However the difference is not that large. The feature at 38.68 km s^{-1} is much reduced in amplitude in these observations.

Figure 5.6 shows the time series for the 6.7 GHz methanol masers. Variability is seen in all the velocity features. Visual inspection suggests that all the velocity features show correlated flares with varying amplitudes. The 33.68 km s^{-1} velocity channel is very weak and shows only small variations. Comparison of Figure 5.6 with Figure 5.1 shows that the variability in the two maser sources at 6.7 GHz show different behaviour. The G12.89+0.64 maser emission at 6.7 GHz shows what appears to be periodic variability.

12.2 GHz Methanol Masers

The averaged 12.2 GHz methanol maser spectrum is shown in figure 5.7. There is strong emission at only one velocity, compared to the 6.7 GHz maser. The average spectrum is very similar to that obtained by Caswell et al. (1995b) apart from the weak emission they detected at 28 km s^{-1} which is not visible in these observations. There is very weak emission at $\sim$38 km s^{-1}. The strong emission at 39 km s^{-1} corresponds to the strongest maser emission at 6.7 GHz.

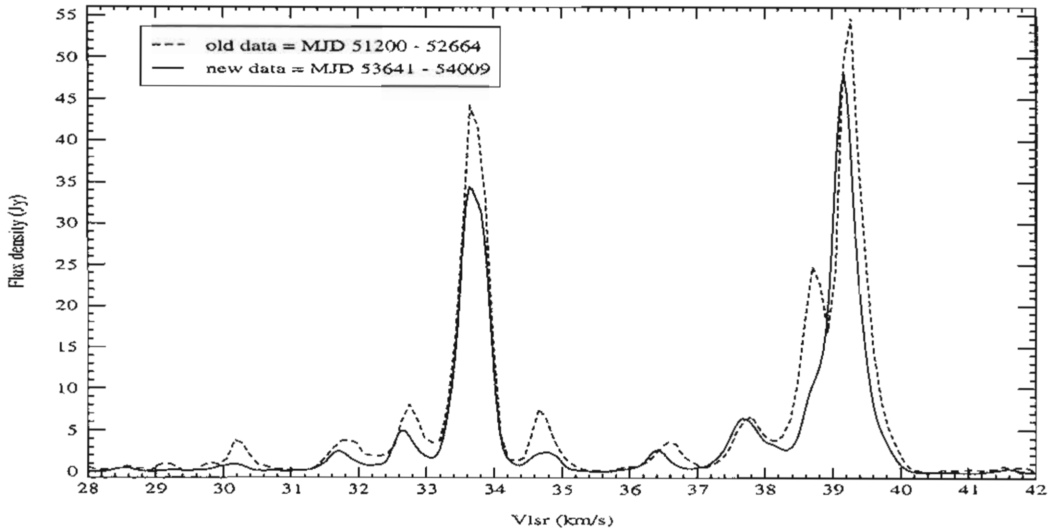

Figure 5.5: The 6.7 GHz average spectra in G12.89+0.49

The time series of the 12.2 GHz methanol masers in G12.89+0.49 is shown in Figure 5.8. The strongest feature at 39.27 km s^{-1} is highly variable. The observations have a gap between modified Julian date (MJD) 53833 and 53858 due to bad weather. Visual inspection of the time series suggest that the masers may be exhibiting periodic variability in contrast to the time series presented in Figure 5.2 showing the variability of G351.42+0.64 masers at 12.2 GHz.

1665 MHz Hydroxyl Masers

Figure 5.9 shows the averaged spectra of 1665 MHz hydroxyl maser for the LCP and RCP data. Only one strong peak is seen in LCP spectrum, the rest are dominated by noise. The RCP spectrum has two strong peaks and also weak peaks that might be noise. The time series for both LCP and RCP are shown in Figure 5.10. The LCP velocity features do not show any significant variability. In contrast, the maser peaks in RCP spectrum show variability with respect to time.

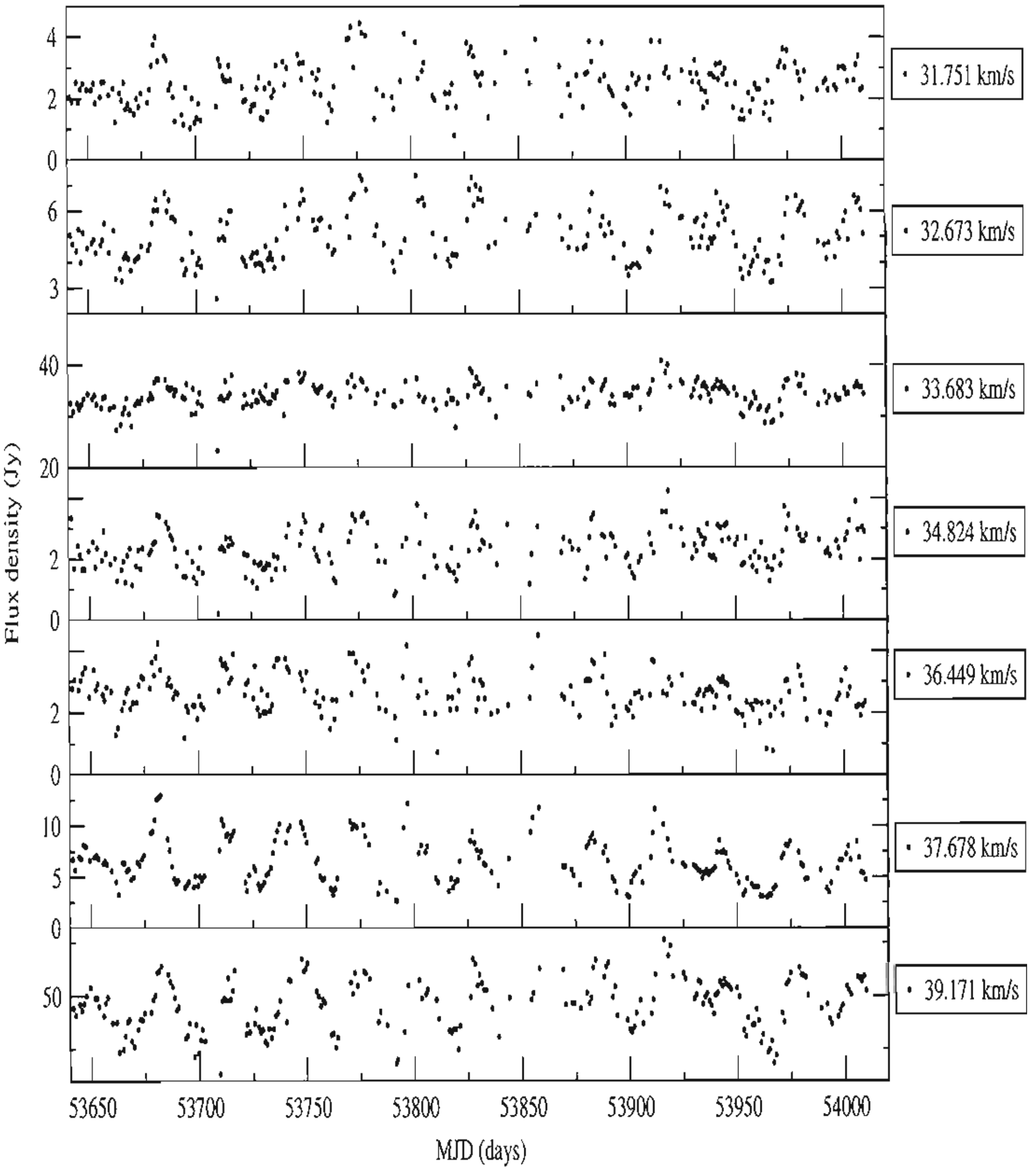

Figure 5.6: The 6.7 GHz methanol maser time series in G12.89+0.49

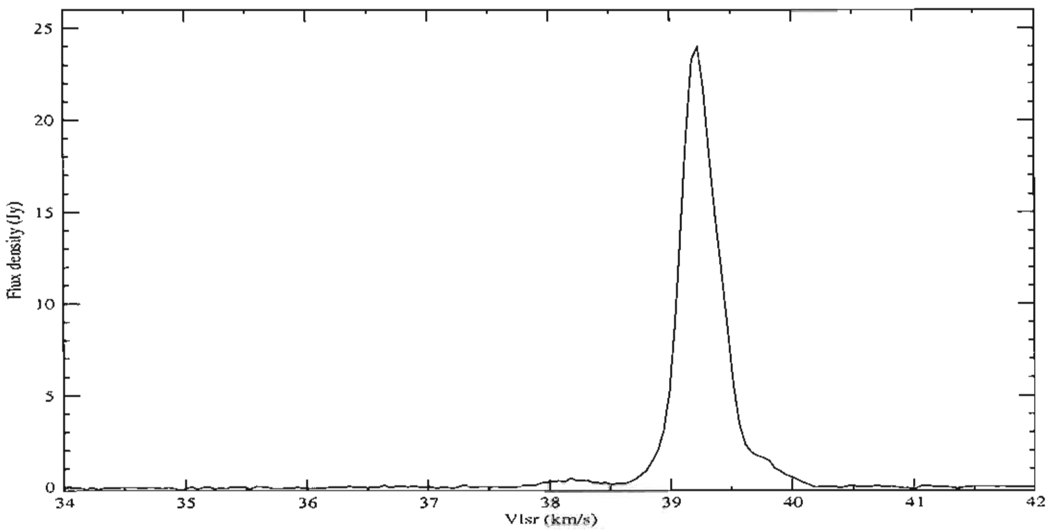

Figure 5.7: The 12.2 GHz maser spectrum in G12.89+0.49

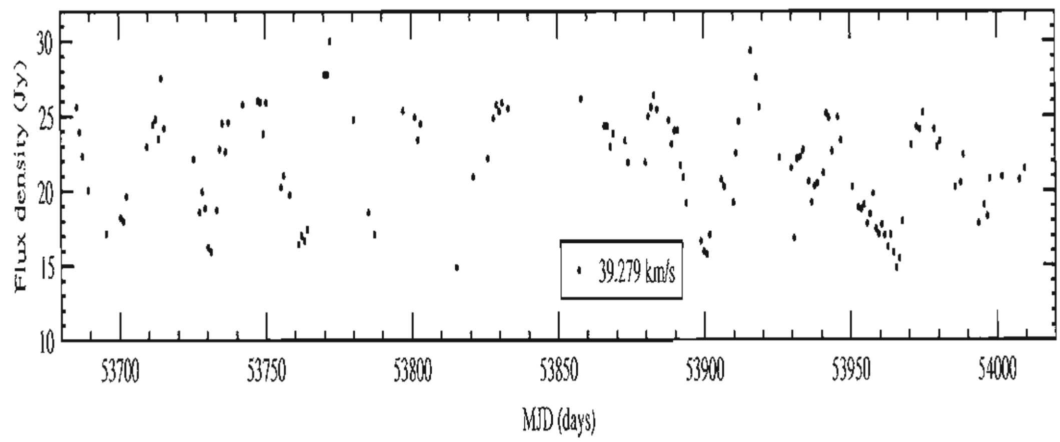

Figure 5.8: The G12.89+0.49 maser time series at 12.2 GHz

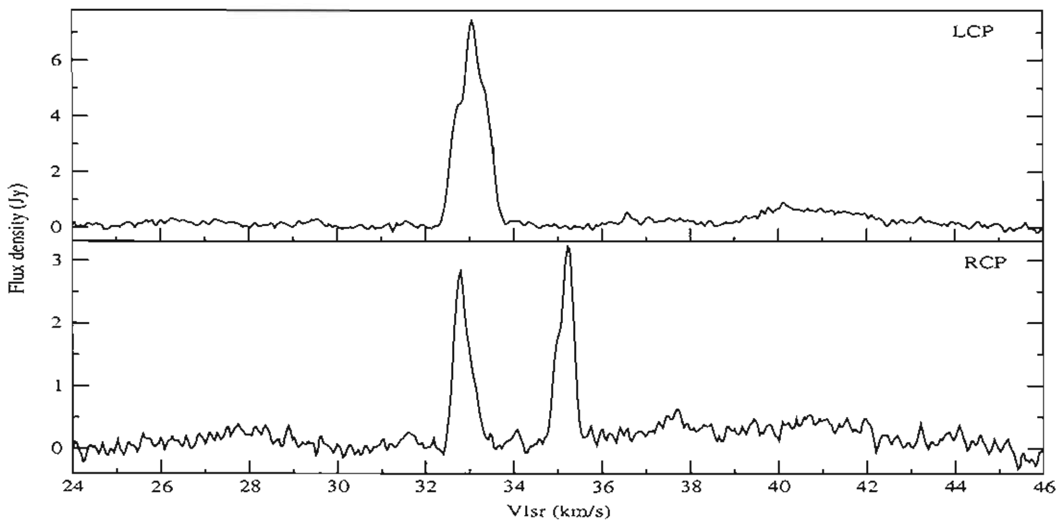

Figure 5.9: 1665 MHz hydroxyl maser spectra in G12.89+0.49

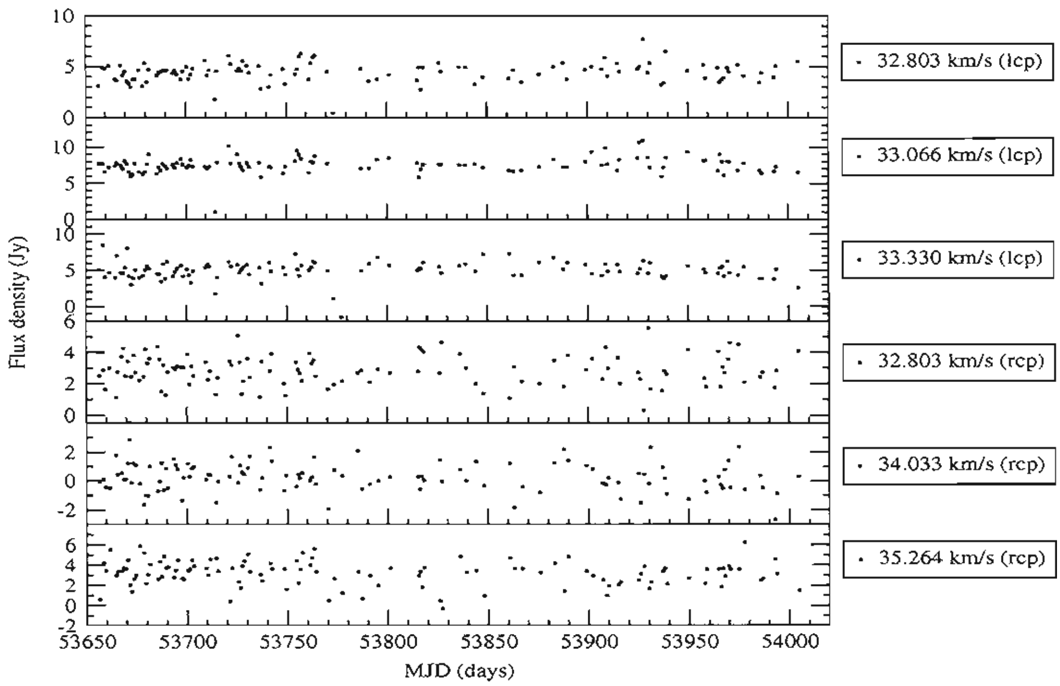

Figure 5.10: Time series for 1665 MHz hydroxyl masers in G12.89+0.49

5.3 Data Analysis

5.3.1 Periodogram using Fourier Transform Method

The analysis to identify the occurrence of periodicity in methanol and hydroxyl masers of G351.42+0.64 and G12.89+0.49 sources was done using the Fourier transform method in the Period04 program (Lenz & Breger, 2005). The periodograms of the time-series at each maser peak were calculated. The frequency and amplitude corresponding to the highest peak of the periodogram were calculated. To determine the significance of the detected peaks a signal-to-noise amplitude ratio (S/N) at each frequency was calculated for each periodogram. According to Breger et al. (1993), peaks are significant if they have S/N of $\gtrsim 4$.

Figures 5.11, 5.12 and 5.13 show the periodograms of G351.42+0.64 at 6.7 GHz, 12.2 GHz, 1665 MHz respectively. The periodograms are all dominated by noise. No periodicity is detected in any of the three maser transitions.

The calculated S/N for the G351.42+0.64 are shown in tables 5.1, 5.2, 5.3 and 5.4. Only few cases occur where the peaks show a S/N of 4 and above, e.g 1665 MHz maser peaks at -10.46 km s^{-1}, -7.65 km s^{-1} and -8.53 km s^{-1} with S/N of 7.5, 4.3 and 5.6 respectively. However, these peaks are dominated by noise and may not be real signals. Thus there is no periodic signal in the comparison source.

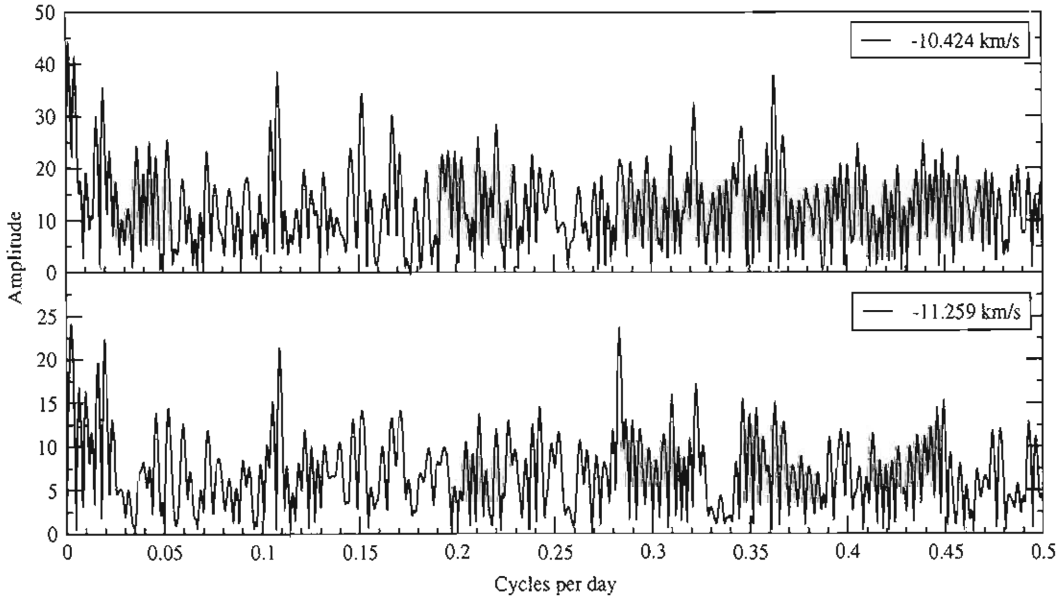

Figure 5.11: G351.42+0.64 periodogram at 6.7 GHz from Fourier analysis

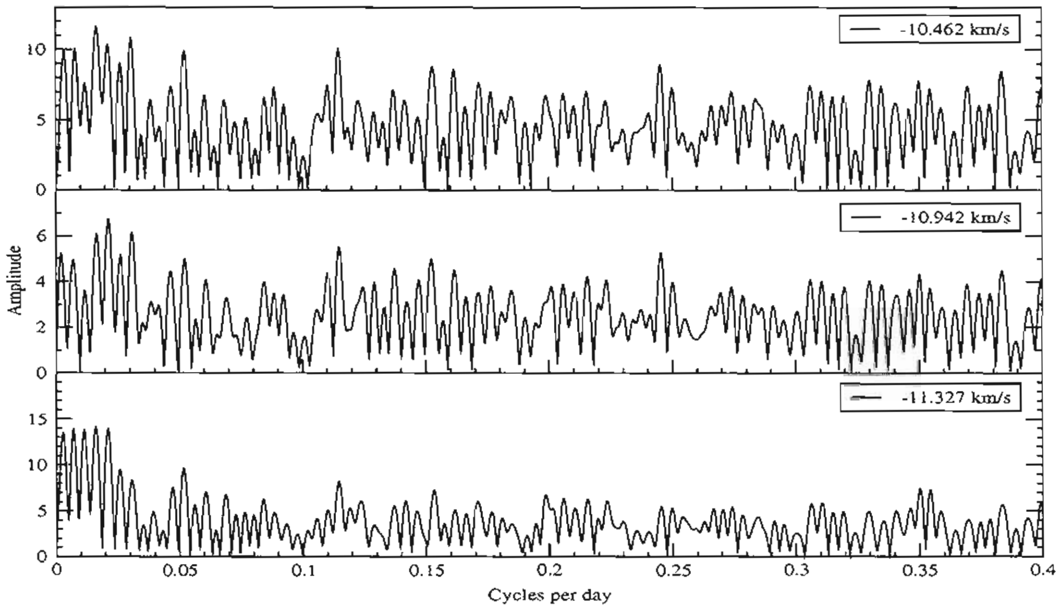

Figure 5.12: G351.42+0.64 periodogram at 12.2 GHz from Fourier analysis

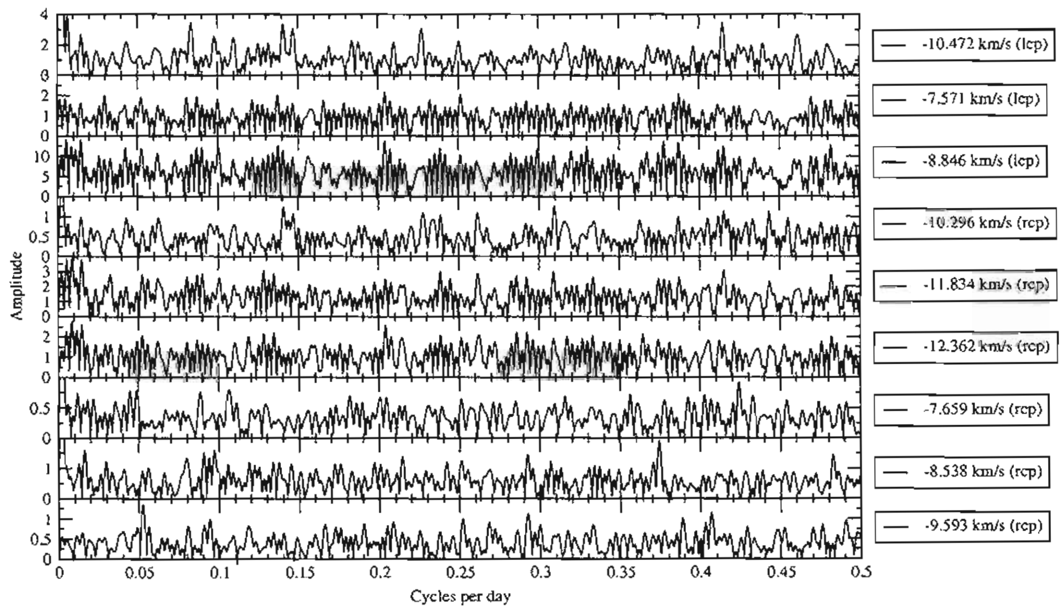

Figure 5.13: G351.42+0.64 periodogram at 1665 MHz from Fourier analysis

Table 5.1: Summary of Fourier analysis of the strongest 6.7 GHz velocity features in G351.42+0.64 periodogram

Maser peaks (km/s)	Freq. (c/d)	P (d)	Amplitude	Noise	S/N
-10.42	0.001635	611	43.858	12.7940	3.4
-11.25	0.002589	386	24.096	7.06586	3.4

Table 5.2: Summary of Fourier analysis of the strongest 12.2 GHz velocity features in G351.42+0.64 periodogram

Maser peaks (km/s)	Freq. (c/d)	P (d)	Amplitude	Noise	S/N
-10.46	0.0166	59	11.629	4.5106	2.5
-10.94	0.0212	46	6.750	2.5095	2.6
-11.32	0.0160	62	14.141	3.6694	3.8

Table 5.3: Summary of Fourier analysis of the strongest 1665 MHz features at LCP in G351.42+0.64 periodogram

Maser peaks (km/s)	Freq. (c/d)	P (d)	Amplitude	Noise	S/N
-10.47	0.002659	376	9.105	1.21154	7.5
-7.57	0.2040	4	2.166	0.9313	2.3
-8.84	0.005458	183	14.0590	6.0439	2.3

G12.89+0.49

6.7 GHz Methanol Masers

Figure 5.14 shows the periodogram for each peak of the 6.7 GHz masers. In contrast to G351.42+0.64, in each periodogram there exists one strong peak. The average frequency of the strong peaks is 0.03432 cycles per day which corresponds to an average period of 29.14 days. Table 5.5 gives the characteristics of the maser peaks. The strong peaks seem to occur nearly at the average frequency for all the features. No higher order harmonics are seen in the periodograms.

Table 5.4: Summary of Fourier analysis of the strongest 1665 MHz features at RCP in G351.42+0.64 periodogram

Maser peaks (km/s)	Freq. (c/d)	P (d)	Amplitude	Noise	S/N
-10.29	0.002939	340	1.909	0.4807	3.9
-11.83	0.008958	111	3.839	1.34467	2.8
-12.36	0.008678	115	2.762	1.0464	2.6
-7.65	0.002379	420	1.525	0.3501	4.3
-8.53	0.001959	510	3.571	0.6301	5.6
-9.59	0.05249	19	1.353	0.4163	3.2

Table 5.5: Summary of Fourier analysis of G12.89+0.49 velocity features at 6.7 GHz

Maser peaks (km/s)	Freq. (c/d)	P (d)	Amplitude	Noise	S/N
31.75	0.03463	28.9	0.5823	0.08240	7.1
32.67	0.03436	29.1	0.8968	0.11009	8.2
33.68	0.03423	29.2	1.3819	0.27946	4.9
34.82	0.03436	29.1	0.5021	0.07605	6.6
36.44	0.03423	29.2	0.4885	0.07440	6.6
37.67	0.03422	29.2	2.1808	0.24178	9.0
39.17	0.03423	29.2	5.6033	0.66096	8.5

12.2 GHz Methanol Masers

The Fourier power spectrum for the 12.2 GHz masers is shown in figure 5.15. Periodicity seems to occur at frequency 0.03454 cycles per day which corresponds to a period of 29.9 days. The fundamental peak shows no higher order harmonics. The signal-to-noise amplitude ratio is 7.970 and it shows that the detected periodicity is significant.

1665 MHz Methanol Masers

Figure 5.16 shows the periodogram for 1665 MHz methanol masers. Like G351.42+0.64, no periodicity is detected in the periodogram. The calculated S/N is shown in table 5.7 and confirms that there is no real periodic signal.

A Fourier analysis of both 6.7 GHz and 12.2 GHz masers in G12.89+0.49 has shown the existence of maser variability with a period between 29 and 30 days.

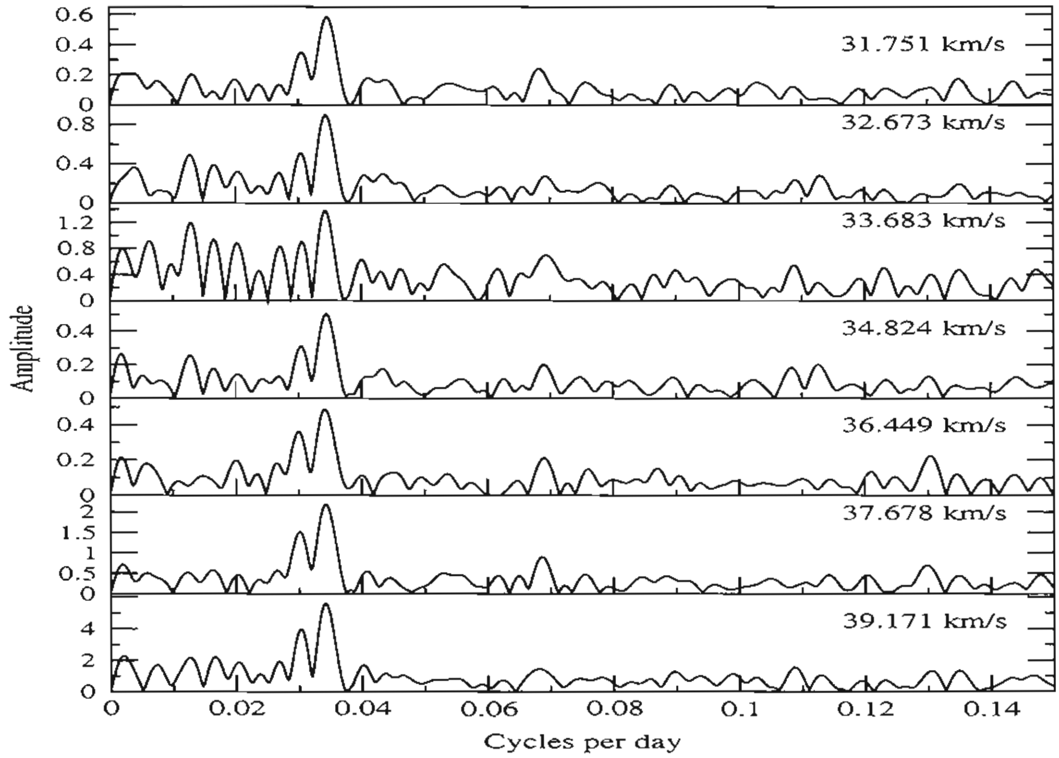

Figure 5.14: 6.7 GHz methanol maser periodogram from Fourier analysis

However, for non-sinusoidal data this method may fail to detect the correct period and thus providing false detection. Hence to cross-check whether the detected periodicity is real, further analysis was done using the epoch folding technique. This also gives an estimate of the uncertainty in the period.

5.3.2 Periodogram using Epoch Folding Technique

The epoch-folding technique (Leahy et al., 1983; Davies, 1990) (see Appendix for discussion and derivation) was used to search for periodicity in the time series of all the masers. The data from each velocity channel were folded modulo a test period and a test statistic was calculated. Since this method is very sensitive to the number of phase bins used, different numbers of phase bins were used ranging from M=5 to M= 15. The data was then averaged to obtain the best fit period which was then used to fold a time-series for each velocity feature.

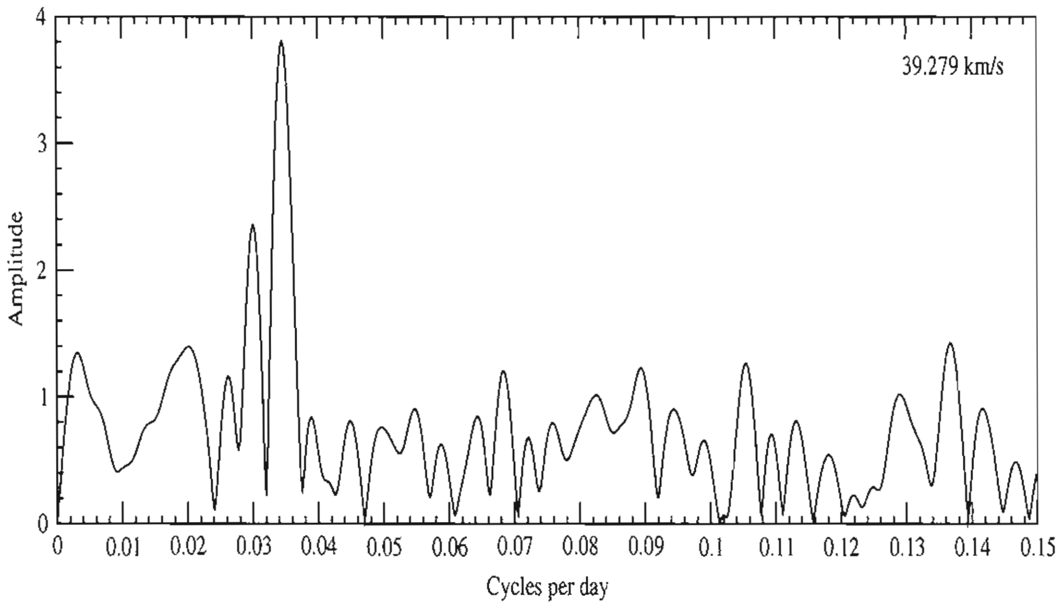

Figure 5.15: 12.2 GHz methanol maser periodogram from Fourier analysis

Table 5.6: Summary of Fourier analysis of 1665 MHz features at RCP in G12.89+0.49

Maser peaks (km/s)	Freq. (c/d)	P (d)	Amplitude	Noise	S/N
32.803	0.3233	3.1	0.444	0.1630	2.7
35.044	0.4648	2.2	0.457	0.1580	2.9
35.264	0.1819	5.5	0.541	0.2015	2.6

G12.89+0.49 Methanol Masers at 6.7 GHz

The periodogram for each velocity channel in the 6.7 GHz masers using different number of bins is presented in Figure 5.17. There are secondary peaks in the periodograms which appear to be caused by some flares starting later than usual. Figure 5.18 shows the averaged periodograms for the maser time series. The periodograms show broad peaks because the cycles do not repeat very well. In order to easily compare the time series, the period derived from the strongest periodogram was used to fold the data.

Figure 5.19 show the folded time series for the velocity channels. The data were folded modulo 29.4 days and the results are plotted in separate cycles. The start point of the cycles is unknown. For convenience, it has been chosen to be at the minima prior to the main flare. Most of the cycles show similar

Table 5.7: Summary of Fourier analysis of 1665 MHz features at LCP in G12.89+0.49

Maser peaks (km/s)	Freq. (c/d)	P (d)	Amplitude	Noise	S/N
32.80	0.0489	20.449	0.534	0.2300	2.3
33.06	0.0491	20.366	0.695	0.2836	2.4
33.33	0.2375	4.219	0.651	0.2367	2.7

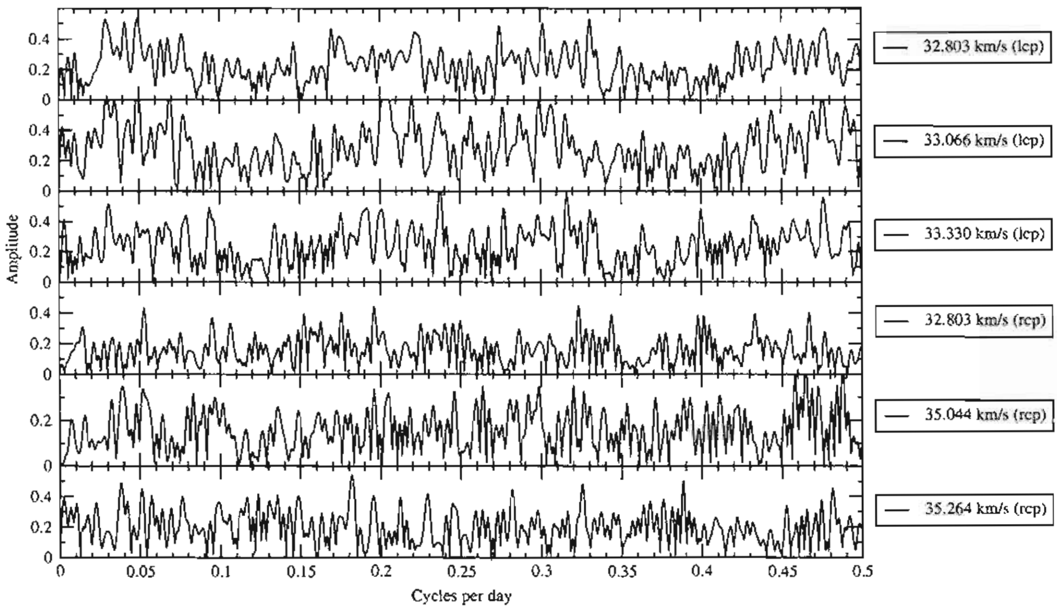

Figure 5.16: G12.89+0.49 periodogram at 1665 MHz from Fourier analysis

amplitudes. The cycles are clear but they do not repeat exactly. All the cycles seem to rise fast over 10 days to the maximum and decay slowly to minimum at 25 days. The secondary period of 32.3 days were folded to check if there is a real signal. The results are shown in Figure 5.20. No clear cycles are seen in the data for the maser peaks at 33.68 and 36.44 when folded modulo 32.3 days. It appears as though there is a phase lag between the different peaks. Further analysis is presented in section 5.5 to confirm this suggestion.

G12.89+0.64 Methanol Masers at 12.2 GHz

Figure 5.21 shows the epoch-folding periodogram of 12.2 GHz masers with different number of phase bins. The averaged periodogram is shown in Figure 5.22. Like its 6.7 GHz counterpart the periodogram shows a broad sec-

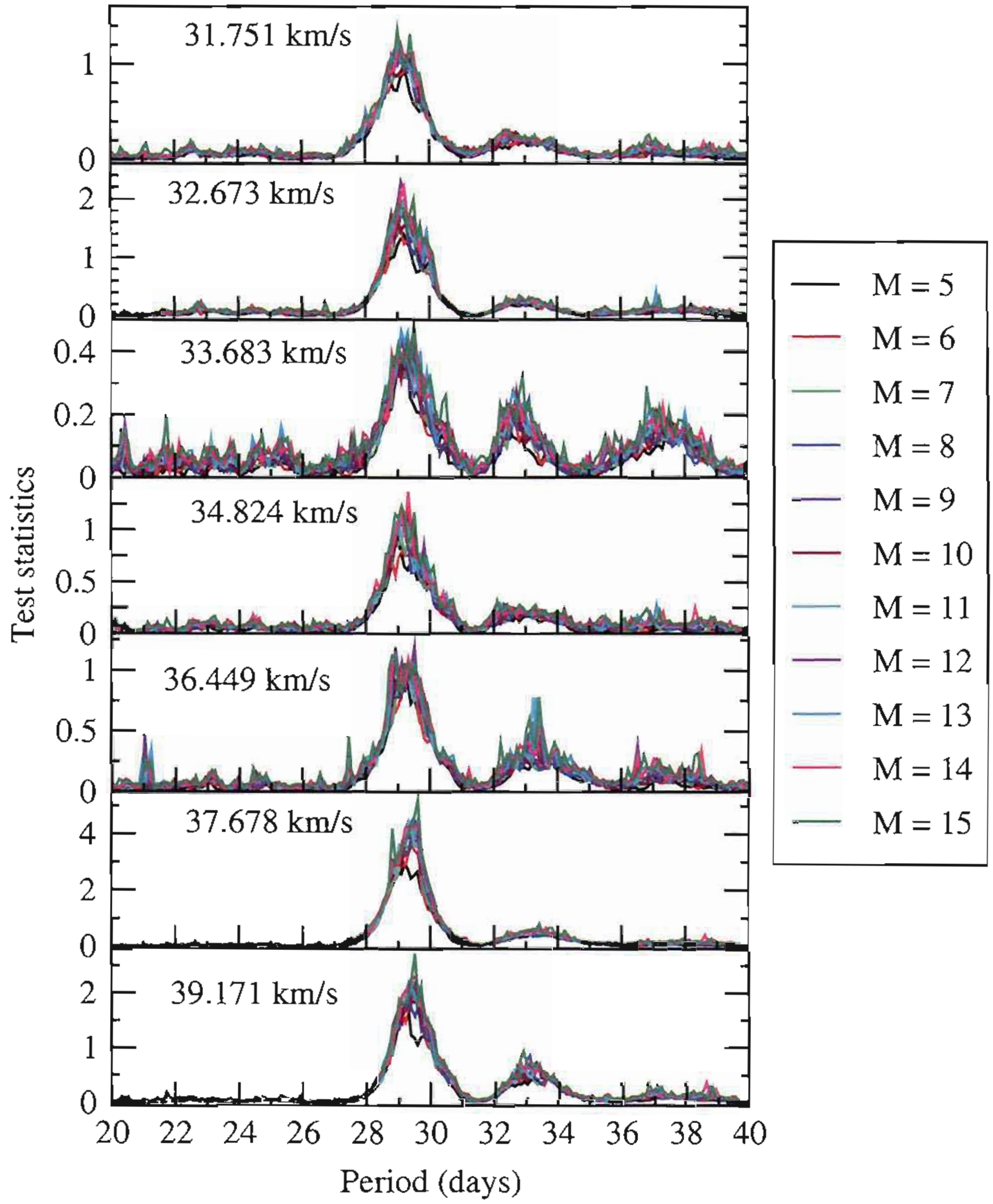

Figure 5.17: 6.7 GHz methanol maser periodogram in G12.89+0.49 from epoch-folding analysis with different numbers of bins

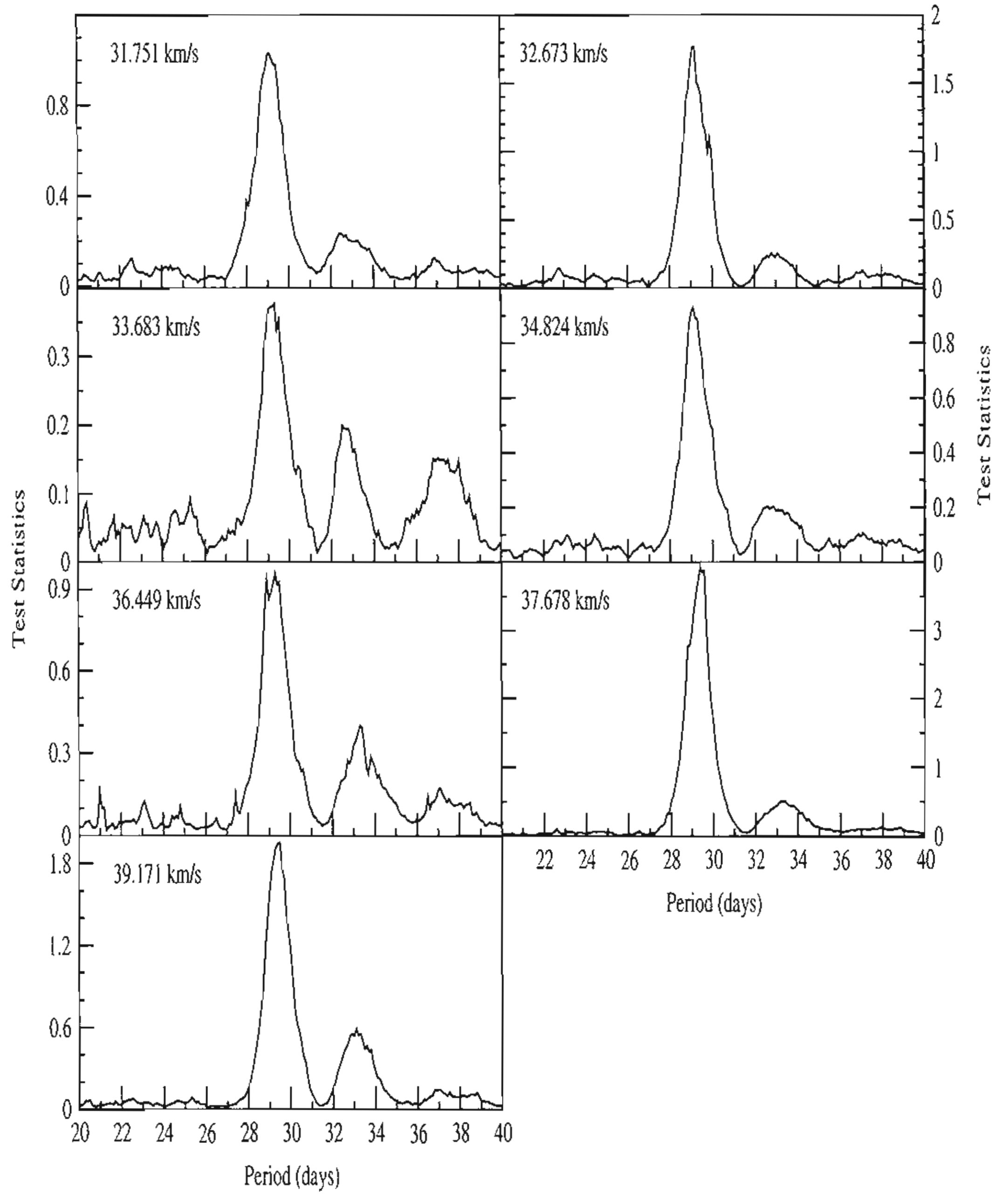

Figure 5.18: Averaged periodogram from epoch-folding analysis for the 6.7 GHz methanol maser features in G12.89+0.49

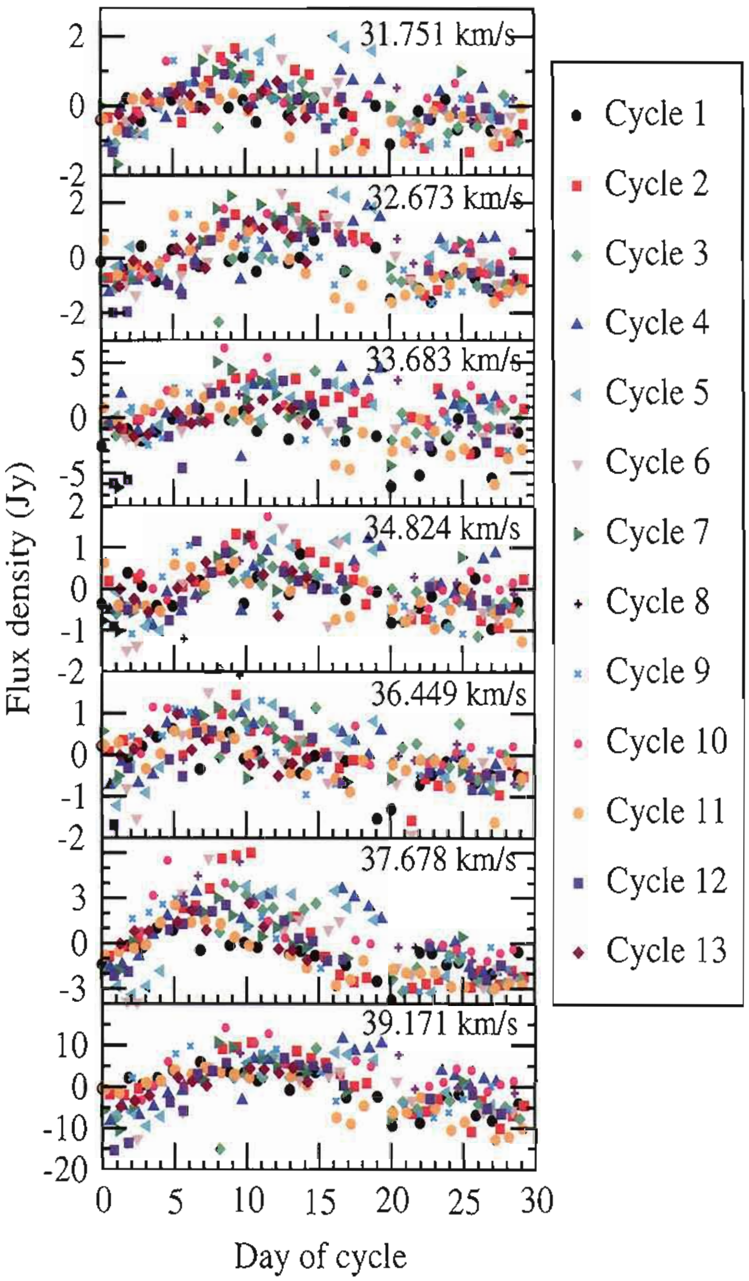

Figure 5.19: 6.7 GHz methanol maser detrended time series folded modulo 29.4 days

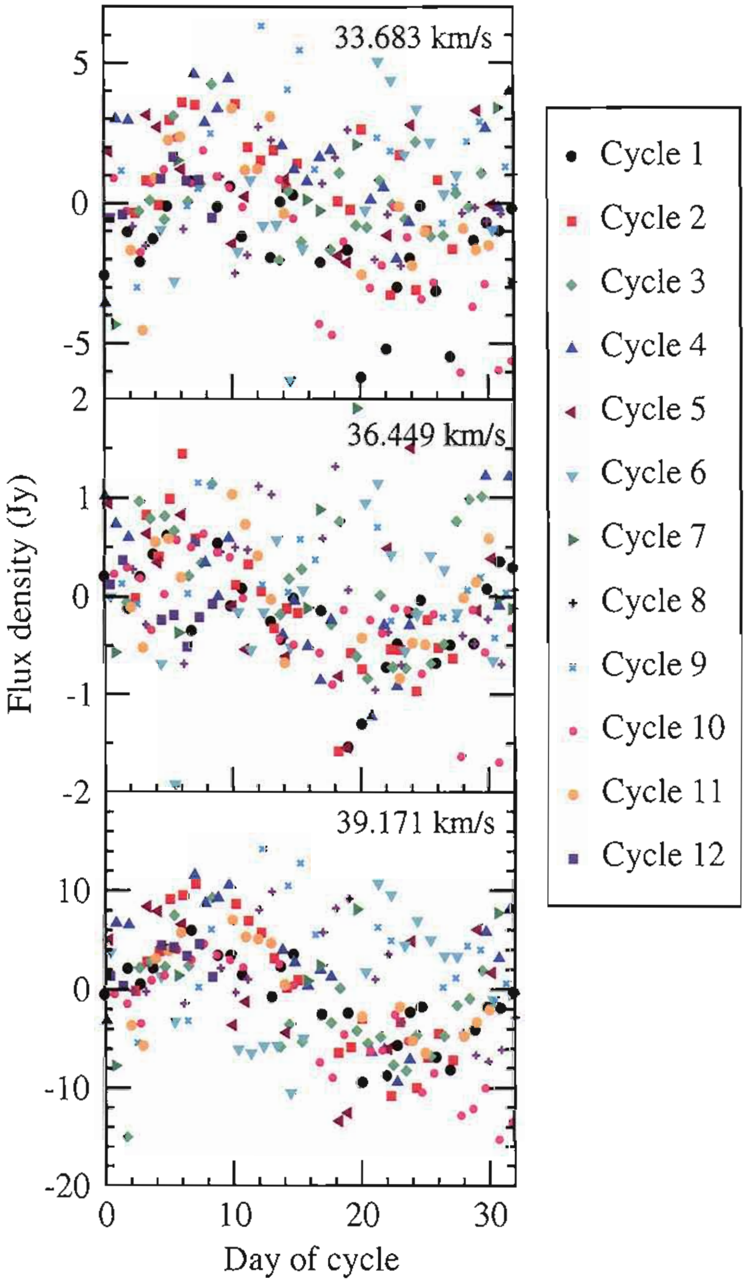

Figure 5.20: 6.7 GHz methanol maser detrended time series folded modulo 32.3 days

ondary peak at about 34 days. Estimation of the highest peak gives a period of 29.3 days and was therefore used to fold the time series. Results of the folded data are shown in Figures 5.23. The cycles begin at different amplitudes, with cycles 1 and 6 being started much later than the others. They tend to rise up fast and drop down slowly. In contrast to the rest of the cycles, cycle 11 lasted shorter than the usual. Most of cycles have similar maximum amplitudes and drop to similar minimum levels.

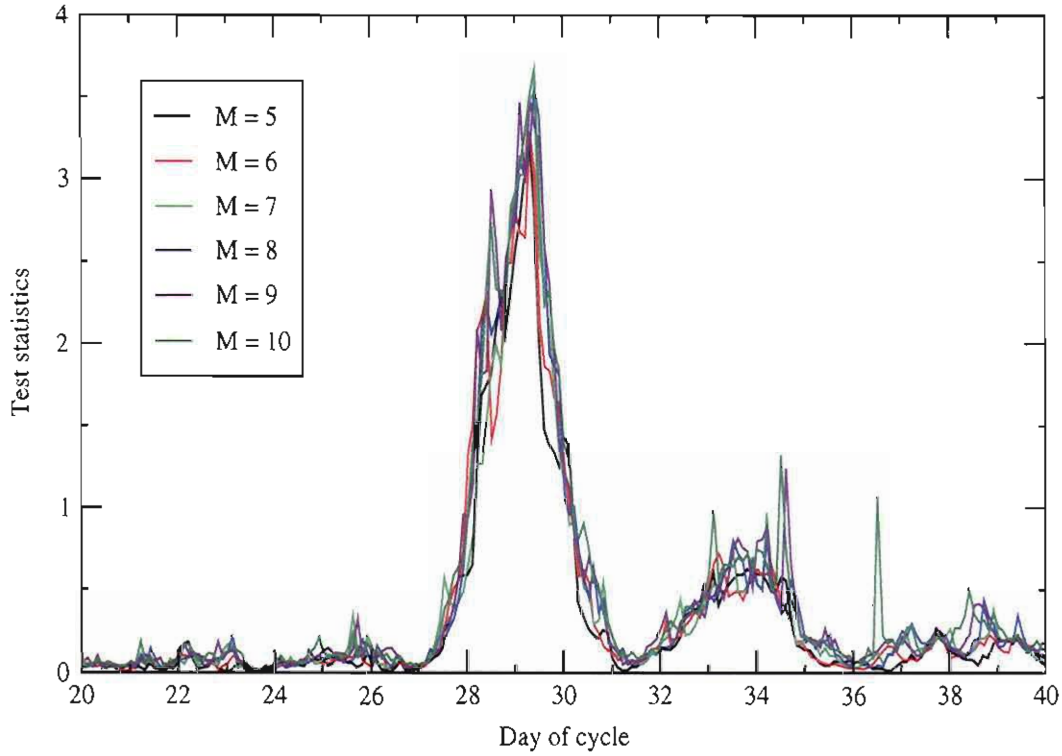

Figure 5.21: 12.2 GHz methanol maser periodogram in G12.89+0.49 from epoch-folding analysis with different number of bins

5.4 Degree of Variability in the 6.7 GHz and 12.2 GHz Masers

The time series of the 6.7 GHz and 12.2 GHz masers show that all the detected velocity features exhibit variability. Simple calculations were performed in order to quantify the degree of variability of these features. These calculations were done by fitting a sinusoidal to each time series and taking the minimum, maximum and mean intensity of the time series. A typical sinusoidal fit is shown in Figure 5.24. Thus the degree of variability was calculated using the

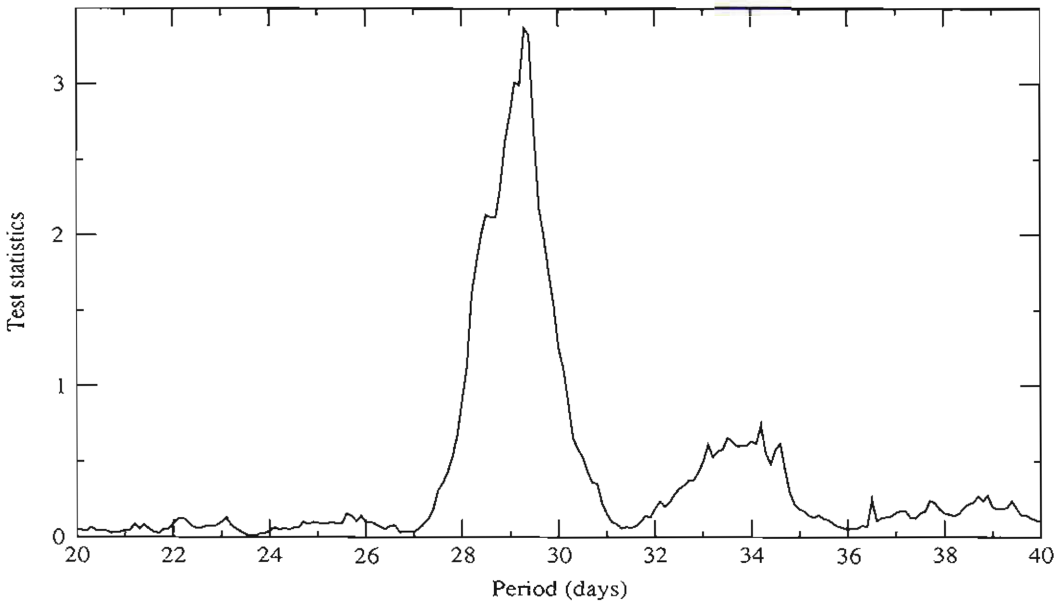

Figure 5.22: 12.2 GHz methanol maser average periodogram in G12.89+0.49 from epoch-folding analysis

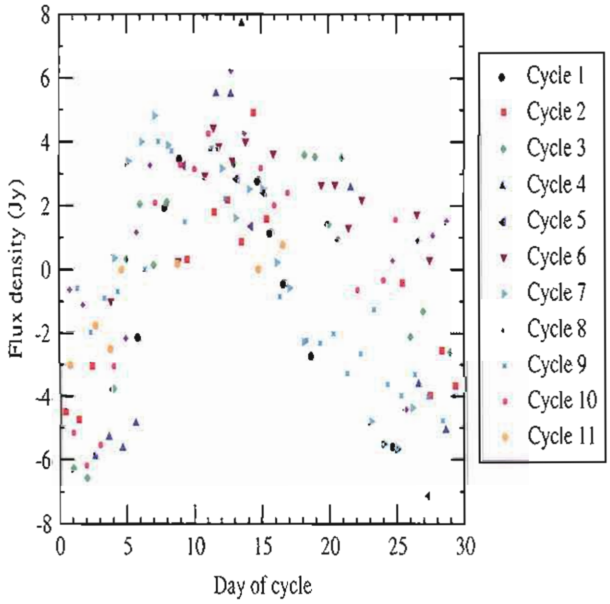

Figure 5.23: 12.2 GHz methanol maser detrended time series folded modulo 29.3 days

formula

$$\text{degree of variability} = \frac{I_{max} - I_{min}}{I_{mean}} \times 100\% \tag{5.1}$$

From Figure 5.24 it can be seen that the I_{max} and I_{min} are more extreme. For

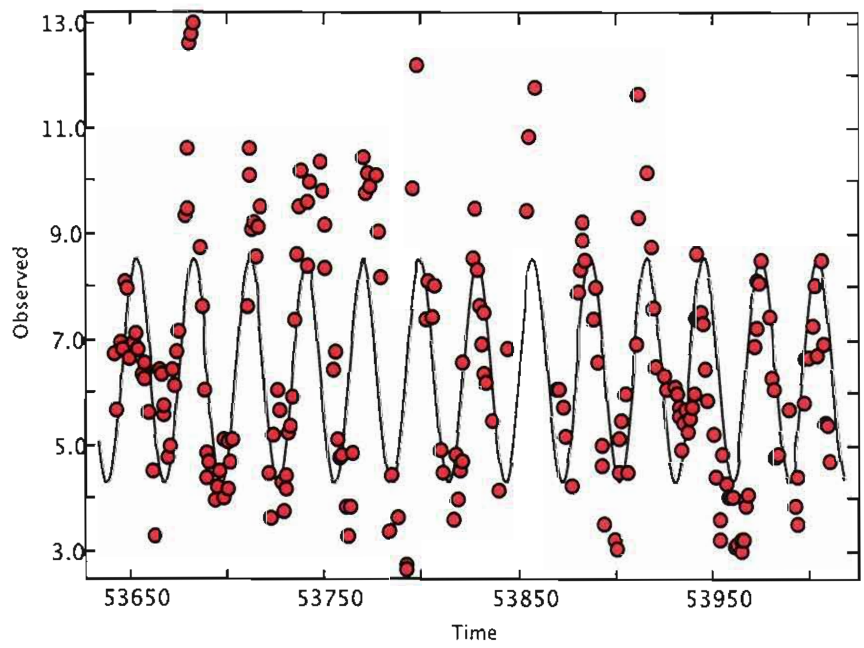

Figure 5.24: Sinusoidal fit to 37.68 km s^{-1} 6.7 GHz maser

convenience only the intensity within the sinusoidal fit was used. The results for the 6.7 GHz and 12.2 GHz maser features are presented in Figure 5.25. The 6.7 GHz maser peaks are shown by the first seven bars from the left and the 12.2 GHz maser peak is the last or the 8th bar. From the histogram it is confirmed that the 33.68 km s^{-1} velocity feature has indeed little variability as suggested earlier. The histogram also shows that most of the 6.7 GHz maser features have variations ranging between 30% to 44% with 62% variations being the highest. The 39.27 km s^{-1} velocity feature in the 12.2 GHz masers shows strong variability with 30% variations compared to its 6.7 GHz maser feature which has only 21% variations.

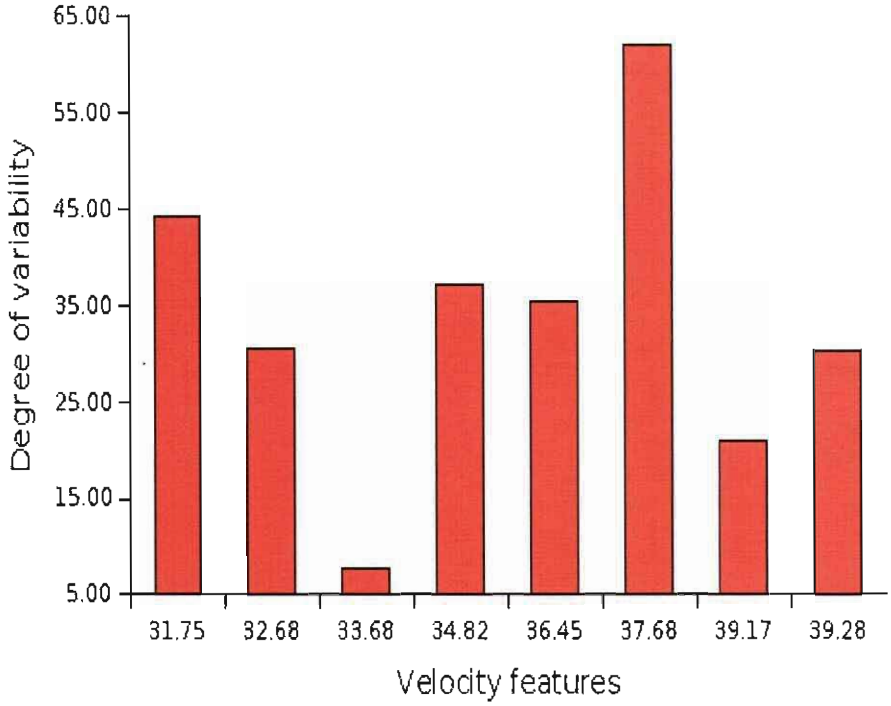

Figure 5.25: Degree of variability. The first seven bars from the left show variability measure for the peaks in 6.7 GHz and the last bar shows the variability measure for 12.2 GHz methanol peak

5.5 Cross-Correlation Analysis

The epoch-folded time series (Figure 5.19) for different peaks at 6.7 GHz in G12.89+0.49 suggest that the peaks might be exhibiting time delays. In order to confirm if there is significant time delays between these peaks, further examinations were done by using the z-transformed discrete correlation function (ZDCF) (Valdes-Galicia & Alexander, 1997).

The results for the 6.7 GHz maser features from the cross-correlation analysis are shown in Figure 5.26. The peak at 39.17 km s^{-1} was used as a reference channel. The results show that there is a strong correlation between all the maser peaks but with no time delay.

Figure 5.27 shows the time series of ~39 km s^{-1} feature at 6.7 GHz and 12.2 GHz. The variability in both masers appear to be in phase and correlated. This is confirmed by a strong correlation obtained from the cross-correlation analysis presented in figure 5.28.

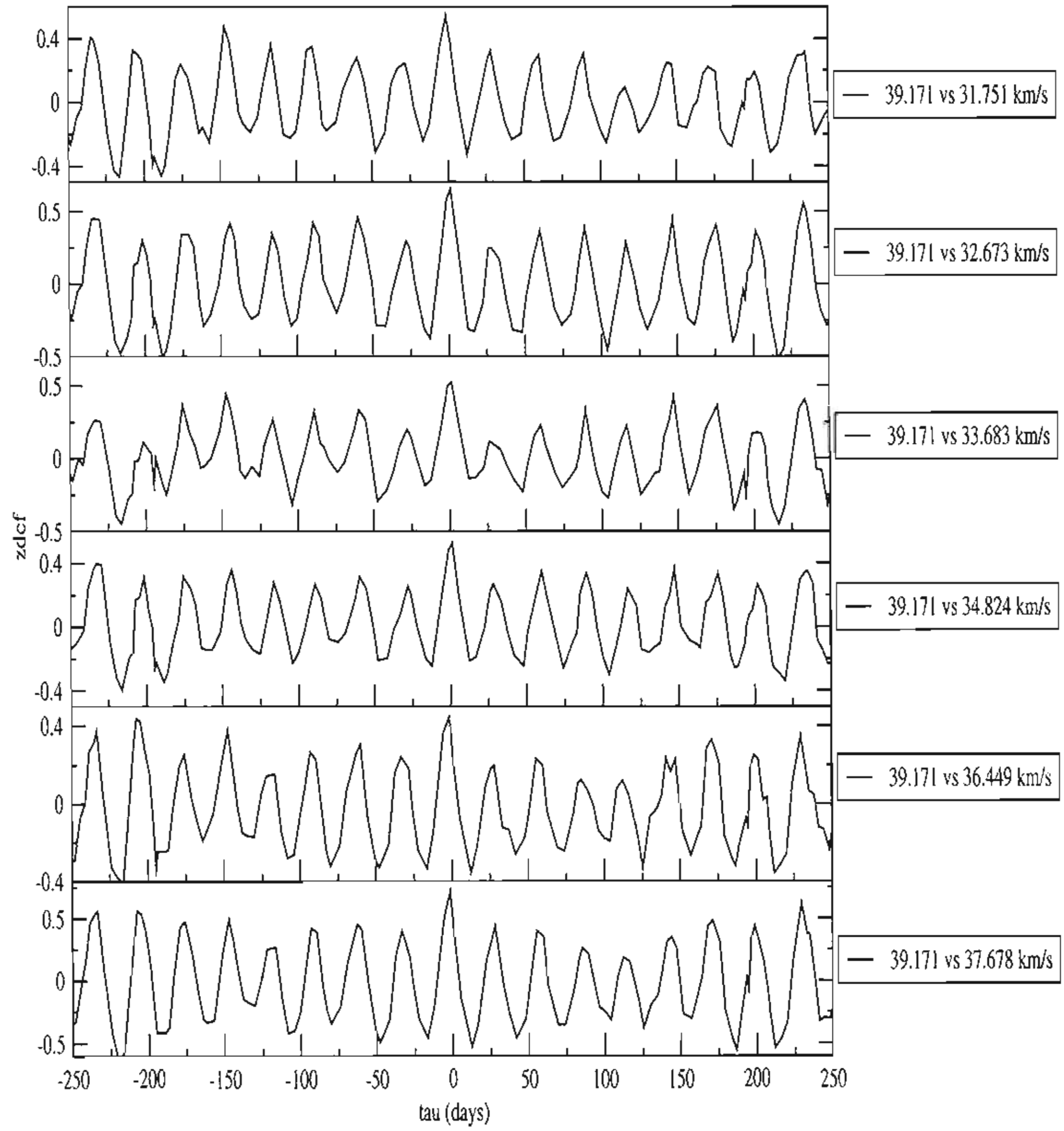

Figure 5.26: Cross correlation between different peaks of 6.7 GHz methanol masers in G12.89+0.49

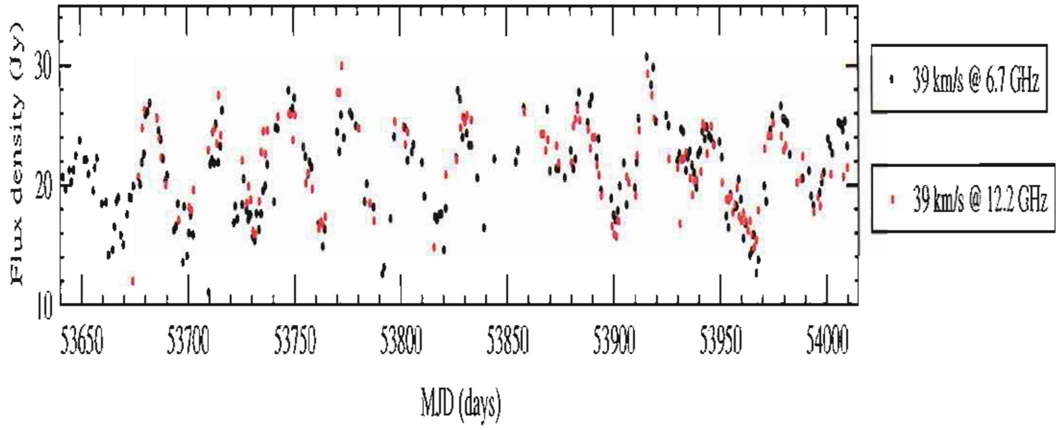

Figure 5.27: Time series of 6.7 GHz and 12.2 GHz masers ~39 km s^{-1} feature in G12.89+0.49

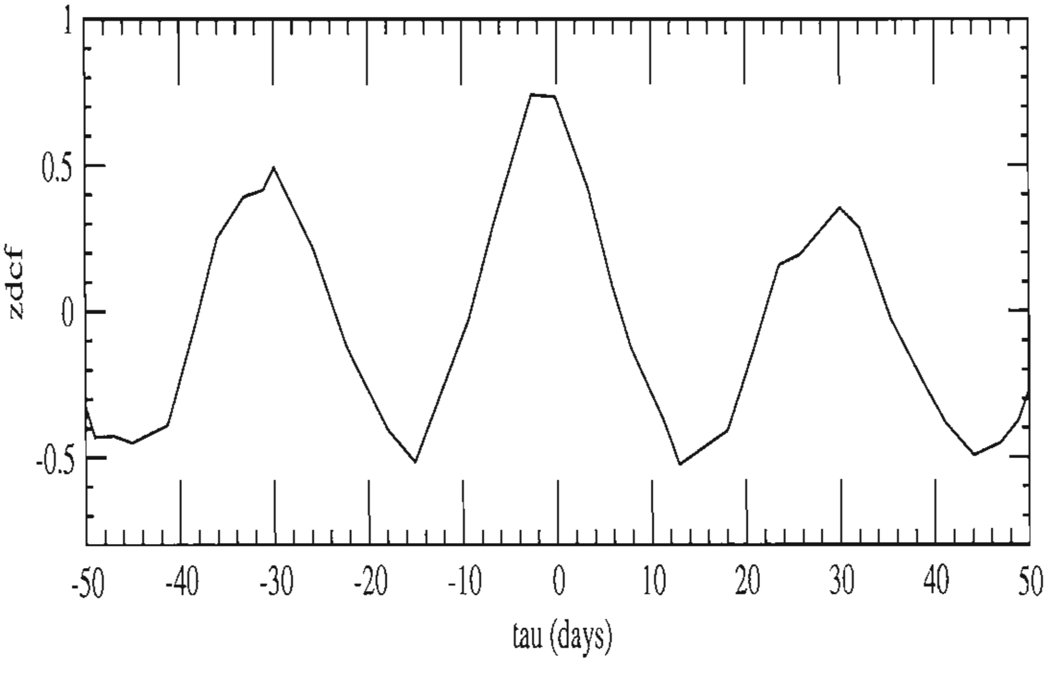

Figure 5.28: Cross-correlation of 6.7 GHz and 12.2 GHz masers at ~39 km s^{-1} feature in G12.89+0.49

5.6 Conclusion

The results presented here show that the reference source G351.42+0.64 shows small variability at 6.7 GHz and 12.2 GHz. No regular variability is seen at 1665 MHz. The detected variability does not show any correlations with G12.89+0.49. The methanol masers at 6.7 GHz in G12.89+0.64 show regular variability. A periodicity analysis using the Fourier transform method shows that the variability occurs at an average period of 29 days. The epoch folding method gives an average period of 30 days. From this, the likely errors in the period can be estimated to be about a day. This is reasonable as it matches the sampling interval. Time series of different peaks of 6.7 GHz in the G12.89+0.64 show strong correlation without any time delay.

The 12.2 GHz methanol masers in G12.89+0.64 star-forming region are highly variable. A period of 29 days was obtained by using the Fourier transform method. The epoch folding method gives a period of 30 days. As for the 6.7 GHz masers, there is an uncertainty of one day. Cross correlation between the strong 12.2 GHz maser peak and the strongest peak at 6.7 GHz shows that the two peaks are correlated with no time delay.

Hydroxyl masers show weak variability in the 1665 MHz masers in the RCP data. The LCP data do not show any significant variability. Further discussion of the variability of the masers is given in the next chapter. The discussion includes the possible mechanisms responsible for the detected variability. Conclusions of this work are also given.

Chapter 6

Discussion and Conclusion

6.1 Summary

The results of the daily monitoring of G12.89+0.49 of the 6.7 GHz methanol masers shows that all the features exhibit correlated flares but varying in strength. One of the features showed small intensity variations. No time delay is seen between the features. An analysis using a Fourier transform method shows that G12.89+0.49 exhibits regular variability with an average period of 29 days. The epoch-folding gives an average period of 30 days. The variability index for the 6.7 GHz maser peaks ranges between 7% and 62%.

The 12.2 GHz methanol masers in the G12.89+0.49 have only one strong peak at 39.27 km s^{-1}. The peak is highly variable with 30% amplitude variation. A Fourier analysis suggests that the source exhibits periodic variability with a period of 29 days. A period of 30 days was obtained when using epoch-folding. A strong correlation exists between the 39 km s^{-1} feature at 12.2 GHz and its 6.7 GHz counterpart.

The 1665 MHz hydroxyl masers at LCP spectrum show no significant variability in. The RCP spectrum seems to show a little variability. No periodicity was detected in either the LCP or RCP maser peaks.

The results obtained from the monitoring of methanol masers suggest that these masers undergo short term regular variations. This is the first time a study has shown that methanol masers exhibit such short term periodicity. The question of interest is, what is the cause of this variability? Some possible mechanisms are discussed below.

6.2 Variability mechanisms in G12.89+0.64

The regular variations of the 6.7 GHz and 12.2 GHz methanol masers in the G12.89+0.49 star-forming region could be caused by pulsating variable stars. The luminosity estimations by Purcell et al. (2006) suggested that the source might be an early B0 type star. Such stars could be β Cephei pulsating stars, but their periods range between 0.1 and 5 days. Hence pulsating stars cannot be a plausible explanation for the periodicity observed in these observations.

Periodicity could be caused by a rotating star with a hot spot as a result of accretion. However, high mass stars are considered to be fast rotators. Their typical rotational velocities range between 50 and 340 km s^{-1} (Penny, 1996). These velocities correspond to rotational periods of 0.6 and 5 days (Stassun et al., 1999). Such periods are much less than the period detected in G12.89+0.49. Therefore, this mechanism cannot easily explain the periodicity in G12.89+0.49.

The periodicity in G12.89+0.49 source could be caused by binary systems. Most high mass stars are formed in clusters and several such stars might have companions. It is possible that the star exciting the masers might also have a companion star. This companion star might be the one causing regular variability as it orbits around a central star.

Disks and outflows systems, which are formed from accretion of molecular material during star formation, have been detected in the G12.89+0.49 star-forming region by Beuther et al. (2005) and Sridharan et al. (2002) respectively. The periodicity in this source could therefore be associated with these systems.

6.3 Conclusions

The 6.7 GHz and 12.2 GHz methanol masers and 1665 MHz hydroxyl masers in the G12.89+0.49 star-forming region were monitored using the 26-m telescope at HartRAO for the period of about ten months. The results show that within the ten months of the study, the methanol masers in 6.7 GHz and 12.2 GHz show regular variations with a period of 29 to 30 days. However, the hydroxyl masers present in this star-forming region do not show variability at LCP, while RCP exhibits weak variations over the monitoring period of this study.

Correlation studies of the velocity features at the 6.7 GHz and 12.2 GHz were done using a dominant velocity feature at 6.7 GHz (corresponding to the 12.2 GHz velocity feature). All the velocity features in 6.7 GHz show a strong correlation with the reference velocity feature. Similarly, the velocity feature at the 12.2 GHz correlates with the reference velocity feature deduced from the 6.7 GHz transition.

It could be interesting to investigate the trend of the periodicity detected in this study. In order to determine whether the period found in the 6.7 GHz and 12.2 GHz maser remains constant for a long period of time or whether the amplitude is changing, further monitoring is required. Long term monitoring of hydroxyl maser in the G12.89+0.49 would also validate the current conclusion that the hydroxyl maser at 1665 MHz does not show variability.

The causes of variability in the G12.89+0.49 source have not been investigated in this study. Earlier studies detected disks and outflow systems in this region. Whether or not these systems are the causative agents of the variability is yet to be proven. It is also not known yet if the G12.89+0.49 region has binary systems. These remaining questions could be addressed if a study on the possible causes of variability of methanol masers in the G12.89+0.49 is conducted. Imaging methanol and hydroxyl masers with high angular resolution such as VLA, VLBA, and VLBI may also be required in order to determine the distribution of maser spots. This is important since it could help determine the angular size, structure, and the exact position of these masers. The results may also be useful in determining if the masers are associated with other nearby objects.

Appendix A

Epoch Folding Method

The epoch-folding technique is applied to unevenly sampled data with low signal-to-noise ratio. Its application does not require any assumptions about the the shape of the pulse in a given time series. In epoch folding the time series is broken up into segments the length of a test period. The segments are overlaid on each other, called folding. If the test period is not the true period then the folded data points appear as a straight line with zero slope. However, if the test period is close to the true period then the data will show a deviation from a constant value and show the characteristic shape of the pulse. A number of test statistics exist to detect when the true period is found. The success of the statistic depends on the characteristics of the time series. One such is the so-called Q^2 statistical test, derived below, based on Leahy et al. (1983).

Let x_i be a time series with N observations, where i=1,2,3,...N. Suppose that the data is grouped into test periods from p_{min} to p_{max}. Now for each test period the data is folded and further divided into M windows. Let j be any window in M. Suppose that x_{kj} is the k^{th} observation in the j^{th} window and n_j is the total number of data points in the same window. The mean and the variance in the j^{th} window is calculated according to

$$\bar{x}_j = \frac{1}{n_j - 1} \sum_{k=1}^{n_j} x_{kj} \qquad (6.1)$$

$$\sigma_j = \frac{1}{n_j - 1} \sum_{k=1}^{n_j} (x_{kj} - \bar{x}_j)^2 \qquad (6.2)$$

Let $\bar{x}_j$ be the mean of the full time series, then

$$\bar{x} = \frac{1}{N - 1} \sum_{i=1}^{N} x_i \qquad (6.3)$$

Similarly, the variance of the full time series is calculated as

$$\sigma = \frac{1}{N - 1} \sum_{i=1}^{N} (x_i - \bar{x})^2 \qquad (6.4)$$

The null hypothesis states that the mean and variance for each window is equal to the total mean and variance of the total number of windows and hence no signal is detected

$$\bar{x}_j = \bar{x} \tag{6.5}$$

$$\sum_{j=1}^{M}(\bar{x}_j - \bar{x}) = 0 \tag{6.6}$$

From Leahy et al. (1983) the epoch folding Q statistic test can be defined as

$$Q^2 = \sum_{j=1}^{M} \frac{(x_{kj} - \bar{x})^2}{\sigma_j^2} \tag{6.7}$$

Using the null hypothesis σ_j^2 can be estimated as

$$\sigma_j^2 \approx \frac{\sigma^2}{n_j} \tag{6.8}$$

Using this approximation to the Q statistic test expression gives

$$Q^2 = \frac{1}{\sigma^2}\sum_{j=1}^{M} n_j(x_{kj} - \bar{x})^2 \tag{6.9}$$

Repeating this calculation for each test creates a periodogram. The Q^2 statistical test depends on the number of windows used. If the number of windows are small the flares may not be detected and hence the periodogram has a high false alarm probability level. Also if there are too many windows and not enough data points some of the bins will be empty and hence give errors.

Since the Q^2 statistical test is easily affected by the binning process it has low sensitivity. Hence it is not reliable when detecting the periodicity in the data with small sample size. For example in masers the Q^2 statistical test may produce broad peaks with frequencies greater than the sampling rate. In this case the waveform may suffer from aliasing. Hence it may be difficult to detected the accurate periodicity. Goedhart (in preparation) found that the periodicity in such data (masers) can be better detected by using the L statistical test defined by Davies (1990) as

$$L = \frac{(N - M)Q^2}{(M - 1)[(N - 1) - Q^2]} \tag{6.10}$$

Bibliography

Anderson N., Watson W. D., 1990, ApJ, 348, L69

Barrett A. H., Schwartz P. R., Waters J. W., 1971, ApJ, 168, L101

Bartkiewicz A., Szymczak M., van Langevelde H. J., 2005, A&A, 442, L61

Batrla W., Matthews H. E., Menten K. M., Walmsley C. M., 1987, Nat, 326, 49

Beuther H., Hunter T. R., Zhang Q., Sridharan T. K., Zhao J.-H., Sollins P., Ho P. T. P., Ohashi N., Su Y. N., Lim J., Liu S.-Y., 2004a, ApJ, 616, L23

Beuther H., Walsh A., Schilke P., Sridharan T. K., Menten K. M., Wyrowski F., 2002, A&A, 390, 289

Beuther H., Zhang Q., Greenhill L. J., Reid M. J., Wilner D., Keto E., Marrone D., Ho P. T. P., Moran J. M., Rao R., Shinnaga H., Liu S.-Y., 2004b, ApJ, 616, L31

Beuther H., Zhang Q., Sridharan T. K., Chen Y., 2005, ApJ, 628, 800

Bonnell I. A., 2002, in ASP Conf. Ser. 267: Hot Star Workshop III: The Earliest Phases of Massive Star Birth, Crowther P., ed., p. 193

Bonnell I. A., Bate M. R., Zinnecker H., 1998, MNRAS, 298, 93

Brebner G. C., Cohen R. J., Heaton B., Davies S. R., 1987, MNRAS, 229, 679

Breger M., Stich J., Garrido R., Martin B., Jiang S. Y., Li Z. P., Hube D. P., Ostermann W., Paparo M., Scheck M., 1993, A&A, 271, 482

Carpenter J. M., 2000, AJ, 120, 3139

Caswell J. L., 1996a, MNRAS, 283, 606

Caswell J. L., 1996b, MNRAS, 279, 79

Caswell J. L., 1997, MNRAS, 289, 203

Caswell J. L., 1998, MNRAS, 297, 215

Caswell J. L., Vaile R. A., Ellingsen S. P., 1995a, Proc. Astron. Soc. Aust., 12, 37

Caswell J. L., Vaile R. A., Ellingsen S. P., Norris R. P., 1995b, MNRAS, 274, 1126

Caswell J. L., Vaile R. A., Ellingsen S. P., Whiteoak J. B., Norris R. P., 1995c, MNRAS, 272, 96

Caswell J. L., Vaile R. A., Forster J. R., 1995d, MNRAS, 277, 210

Cesaroni R., 1990, 233, 513

Cesaroni R., Felli M., Jenness T., Neri R., Olmi L., Robberto M., Testi L., Walmsley C. M., 1999, A&A, 345, 949

Cesaroni R., Walmsley C. M., Churchwell E., 1992, 256, 618

Cheung A. C., Rank D. M., Townes C. H., Thornton D. D., Welch W. J., 1969, Nat, 221, 626

Churchwell E., 2002, ARA&A, 40, 27

Clegg A. W., Cordes J. M., 1991, ApJ, 374, 150

Codella C., Moscadelli L., 2000, A&A, 362, 723

Cohen R. J., Baart E. E., Jonas J. L., 1988, MNRAS, 231, 205

Cragg D. M., Sobolev A. M., Godfrey P. D., 2002, MNRAS, 331, 521

Cragg D. M., Sobolev A. M., Godfrey P. D., 2005, MNRAS, 360, 533

Davies S. R., 1990, MNRAS, 244, 93

De Buizer J. M., 2003, MNRAS, 341, 277

De Buizer J. M., Radomski J. T., Telesco C. M., Piña R. K., 2005a, in IAU Symposium, Vol. 227, Massive Star Birth: A Crossroads of Astrophysics, Cesaroni R., Felli M., Churchwell E., Walmsley M., eds., pp. 180–185

De Buizer J. M., Radomski J. T., Telesco C. M., Piña R. K., 2005b, ApJS, 156, 179

De Pree C. G., Wilner D. J., Deblasio J., Mercer A. J., Davis L. E., 2005, ApJ, 624, L101

Dobbs C. L., Bonnell I. A., Pringle J. E., 2006, MNRAS, 371, 1663

Dodson R., Ojha R., Ellingsen S. P., 2004, MNRAS, 351, 779

Durisen R. H., Mejia A. C., Pickett B. K., Hartquist T. W., 2001, ApJ, 563, L157

Elitzur M., 1992, ARA&A, 30, 75

Ellingsen S. P., 2006, ApJ, 638, 241

Ellingsen S. P., Norris R. P., McCulloch P. M., 1996a, MNRAS, 279, 101

Ellingsen S. P., von Bibra M. L., McCulloch P. M., Norris R. P., Deshpande A. A., Phillips C. J., 1996b, MNRAS, 280, 378

Etoka S., Cohen R. J., Gray M. D., 2005, MNRAS, 360, 1162

Fiebig D., Duschl W. J., Menten K. M., Tscharnuter W. M., 1996, A&A, 310, 199

Forster J. R., Caswell J. L., 2000, ApJ, 530, 371

Furuya R. S., Cesaroni R., Codella C., Testi L., Bachiller R., Tafalla M., 2002, A&A, 390, L1

Gaylard M. J., MacLeod G. C., 1993, MNRAS, 262, 43

Gaylard M. J., MacLeod G. C., van der Walt D. J., 1994, MNRAS, 269, 257

Goedhart S., Gaylard M. J., van der Walt D. J., 2004, MNRAS, 355, 553

Gwinn C. R., 1994, ApJ, 429, 253

Habing H. J., Israel F. P., 1979, ARA&A, 17, 345

Harvey-Smith L., Cohen R. J., 2006, MNRAS, 371, 1550

Jaffe D. T., Guesten R., Downes D., 1981, ApJ, 250, 621

Kemball A. J., Gaylard M. J., Nicolson G. D., 1988, ApJ, 331, L37

Krumholz M. R., Klein R. I., McKee C. F., 2005, in IAU Symposium, Vol. 227, Massive Star Birth: A Crossroads of Astrophysics, Cesaroni R., Felli M., Churchwell E., Walmsley M., eds., pp. 231–236

Kumar M. S. N., Bachiller R., Davis C. J., 2002, ApJ, 576, 313

Leahy D. A., Darbro W., Elsner R. F., Weisskopf M. C., Kahn S., Sutherland P. G., Grindlay J. E., 1983, ApJ, 266, 160

Lekht E. E., Mendoza-Torres E., Sorochenko R. L., 1995, ApJ, 443, 222

Lenz P., Breger M., 2005, Communications in Asteroseismology, 146, 53

Lin D. N. C., Pringle J. E., 1990, ApJ, 358, 515

MacLeod G. C., Gaylard M. J., 1996, MNRAS, 280, 868

MacLeod G. C., Gaylard M. J., Nicolson G. D., 1992, MNRAS, 254, 1P

MacLeod G. C., Gaylard M. J., Scalise Jr. E., Hughes V. A., 1993, LNP Vol. 412: Astrophysical Masers, 412, 116

MacLeod G. C., Scalise E. J., Saedt S., Galt J. A., Gaylard M. J., 1998, AJ, 116, 1897

Maeder A., Behrend R., 2002, in ASP Conf. Ser. 267: Hot Star Workshop III: The Earliest Phases of Massive Star Birth, Crowther P., ed., p. 179

Malmberg D., de Angeli F., Davies M. B., Church R. P., Mackey D., Wilkinson M. I., 2007, MNRAS, 378, 1207

Mason B. D., Hartkopf W. I., Gies D. R., McAlister H. A., Bagnuolo Jr. W. G., 1996, in Astronomical Society of the Pacific Conference Series, Vol. 90, The Origins, Evolution, and Destinies of Binary Stars in Clusters, Milone E. F., Mermilliod J.-C., eds., p. 40

McKee C. F., Tan J. C., 2003, ApJ, 585, 850

Melnick G. J., Menten K. M., Phillips T. G., 1993, in Bulletin of the American Astronomical Society, Vol. 25, Bulletin of the American Astronomical Society, p. 926

Menten K., 1991a, in ASP Conf. Ser. 16: Atoms, Ions and Molecules: New Results in Spectral Line Astrophysics, Haschick A. D., Ho P. T. P., eds., p. 119

Menten K. M., 1991b, ApJ, 380, L75

Menten K. M., 1996, in IAU Symp. 178: Molecules in Astrophysics: Probes & Processes, van Dishoeck E. F., ed., p. 163

Menten K. M., Melnick G. J., Phillips T. G., 1990, ApJ, 350, L41

Menten K. M., Reid M. J., Pratap P., Moran J. M., Wilson T. L., 1992, ApJ, 401, L39

Minier V., Booth R. S., Conway J. E., 2000, A&A, 362, 1093

Moscadelli L., Menten K. M., Walmsley C. M., Reid M. J., 2002, ApJ, 564, 813

Norris R. P., Byleveld S. E., Diamond P. J., Ellingsen S. P., Ferris R. H., Gough R. G., Kesteven M. J., McCulloch P. M., Phillips C. J., Reynolds J. E., Tzioumis A. K., Takahashi Y., Troup E. R., Wellington K. J., 1998, ApJ, 508, 275

Norris R. P., Whiteoak J. B., Caswell J. L., Wieringa M. H., Gough R. G., 1993, ApJ, 412, 222

Ott M., Witzel A., Quirrenbach A., Krichbaum T. P., Standke K. J., Schalinski C. J., Hummel C. A., 1994, A&A, 284, 331

Penny L. R., 1996, ApJ, 463, 737

Purcell C. R., Balasubramanyam R., Burton M. G., Walsh A. J., Minier V., Hunt-Cunningham M. R., Kedziora-Chudczer L. L., Longmore S. N., Hill T., Bains I., Barnes P. J., Busfield A. L., Calisse P., Crighton N. H. M., Curran S. J., Davis T. M., Dempsey J. T., Derragopian G., Fulton B., Hidas M. G., Hoare M. G., Lee J.-K., Ladd E. F., Lumsden S. L., Moore T. J. T., Murphy M. T., Oudmaijer R. D., Pracy M. B., Rathborne J., Robertson S., Schultz A. S. B., Shobbrook J., Sparks P. A., Storey J., Travouillion T., 2006, MNRAS, 367, 553

Ramachandran R., Deshpande A. A., Goss W. M., 2006, ApJ, 653, 1314

Schutte A. J., van der Walt D. J., Gaylard M. J., MacLeod G. C., 1993, MNRAS, 261, 783

Sewilo M., Churchwell E., Kurtz S., Goss W. M., Hofner P., 2004, ApJ, 605, 285

Shepherd D. S., Churchwell E., 1996, ApJ, 472, 225

Shu F. H., Adams F. C., Lizano S., 1987, ARA&A, 25, 23

Sobolev A. M., 1993, Astronomy Letters, 19, 293

Sobolev A. M., Cragg D. M., Godfrey P. D., 1997, A&A, 324, 211

Sobolev A. M., Deguchi S., 1994, A&A, 291, 569

Sridharan T. K., Beuther H., Schilke P., Menten K. M., Wyrowski F., 2002, ApJ, 566, 931

Stark A. A., Lee Y., 2005, ApJ, 619, L159

Stassun K. G., Mathieu R. D., Mazeh T., Vrba F. J., 1999, AJ, 117, 2941

Szymczak M., Kus A. J., Hrynek G., Kĕpa A., Pazderski E., 2002, A&A, 392, 277

Valdes-Galicia J. F., Alexander P., 1997, Sol. Phys., 176, 327

Voronkov M. A., Brooks K. J., Sobolev A. M., Ellingsen S. P., Ostrovskii A. B., Caswell J. L., 2006, MNRAS

Walsh A. J., Burton M. G., Hyland A. R., Robinson G., 1998, MNRAS, 301, 640

Walsh A. J., Hyland A. R., Robinson G., Burton M. G., 1997, MNRAS, 291, 261

Walsh A. J., Lee J.-K., Burton M. G., 2002, MNRAS, 329, 475

Walsh A. J., Macdonald G. H., Alvey N. D. S., Burton M. G., Lee J.-K., 2003, A&A, 410, 597

Weaver H., Williams D. R. W., Dieter N. H., Lum W. T., 1965, Nat, 208, 29

Wink J. E., Duvert G., Guilloteau S., Gusten R., Walmsley C. M., Wilson T. L., 1994, A&A, 281, 505

Yorke H. W., 2004, in IAU Symposium, Vol. 221, Star Formation at High Angular Resolution, Burton M., Jayawardhana R., Bourke T., eds., p. 141

Yorke H. W., Kruegel E., 1977, A&A, 54, 183

Yorke H. W., Sonnhalter C., 2002, ApJ, 569, 846

Zapata L. A., Rodríguez L. F., Ho P. T. P., Beuther H., Zhang Q., 2006, AJ, 131, 939